



HAL
open science

Spectral signatures of H-rich material stripped from a non-degenerate companion by a Type Ia supernova

Luc Dessart, Douglas C. Leonard, Jose L. Prieto

► **To cite this version:**

Luc Dessart, Douglas C. Leonard, Jose L. Prieto. Spectral signatures of H-rich material stripped from a non-degenerate companion by a Type Ia supernova. *Astronomy and Astrophysics - A&A*, 2020, 638, pp.A80. 10.1051/0004-6361/202037854 . hal-02892072

HAL Id: hal-02892072

<https://hal.sorbonne-universite.fr/hal-02892072>

Submitted on 7 Jul 2020

HAL is a multi-disciplinary open access archive for the deposit and dissemination of scientific research documents, whether they are published or not. The documents may come from teaching and research institutions in France or abroad, or from public or private research centers.

L'archive ouverte pluridisciplinaire **HAL**, est destinée au dépôt et à la diffusion de documents scientifiques de niveau recherche, publiés ou non, émanant des établissements d'enseignement et de recherche français ou étrangers, des laboratoires publics ou privés.

Spectral signatures of H-rich material stripped from a non-degenerate companion by a Type Ia supernova

Luc Dessart¹, Douglas C. Leonard², and Jose L. Prieto^{3,4}

¹ Institut d'Astrophysique de Paris, CNRS-Sorbonne Université, 98bis boulevard Arago, 75014 Paris, France
e-mail: dessart@iap.fr

² Department of Astronomy, San Diego State University, San Diego, CA 92182-1221, USA

³ Núcleo de Astronomía de la Facultad de Ingeniería y Ciencias, Universidad Diego Portales, Av. Ejército 441 Santiago, Chile

⁴ Millennium Institute of Astrophysics, Santiago, Chile

Received 29 February 2020 / Accepted 8 April 2020

ABSTRACT

The single-degenerate scenario for Type Ia supernovae should yield metal-rich ejecta that enclose some stripped material from the non-degenerate H-rich companion star. We present a large grid of non-local thermodynamic equilibrium steady-state radiative transfer calculations for such hybrid ejecta and provide analytical fits for the H α luminosity and equivalent width. Our set of models covers a range of masses for ⁵⁶Ni and the ejecta, for the stripped material (M_{st}), and post-explosion epochs from 100 to 300 d. The brightness contrast between stripped material and metal-rich ejecta challenges the detection of H I and He I lines prior to ~ 100 d. Intrinsic and extrinsic optical depth effects also influence the radiation emanating from the stripped material. This inner denser region is marginally thick in the continuum and optically thick in all Balmer lines. The overlying metal-rich ejecta blanket the inner regions, completely below about 5000 Å, and more sparsely at longer wavelengths. As a consequence, H β should not be observed for all values of M_{st} up to at least 300 days, while H α should be observed after ~ 100 d for all $M_{\text{st}} \geq 0.01 M_{\odot}$. Observational non-detections capable of limiting the H α equivalent width to < 1 Å set a formal upper limit of $M_{\text{st}} < 0.001 M_{\odot}$. This contrasts with the case of circumstellar-material (CSM) interaction, not subject to external blanketing, which should produce H α and H β lines with a strength dependent primarily on CSM density. We confirm previous analyses that suggest low values of order $0.001 M_{\odot}$ for M_{st} to explain the observations of the two Type Ia supernovae with nebular-phase H α detection, in conflict with the much greater stripped mass predicted by hydrodynamical simulations for the single-degenerate scenario. A more likely solution is the double-degenerate scenario, together with CSM interaction, or enclosed material from a tertiary star in a triple system or from a giant planet.

Key words. radiative transfer – supernovae: general

1. Introduction

Unambiguous signatures of the single-degenerate scenario for Type Ia supernovae (SNe Ia) are much desired but hard to secure. One such signature is the identification of material stripped from the companion star by the SN Ia ejecta. Analytic explorations (Wheeler et al. 1975; Chugai 1986) and numerical simulations (Marietta et al. 2000; Pakmor et al. 2008; Liu et al. 2012; Pan et al. 2012; Liu & Stancliffe 2017) of such a scenario have been performed in recent decades and have yielded similar conclusions. The key signatures are that 0.1 – $0.5 M_{\odot}$ of material should systematically be stripped from the non-degenerate companion star, asymmetrically distributed but limited to low velocities below about 1000 km s^{-1} in the resulting ejecta. The main radiative signature for this scenario is proposed to be the appearance at late times of a narrow and strong H α line on top of a normal SN Ia spectrum (Chugai 1986; Mattila et al. 2005; Botyánszki et al. 2018). More sophisticated and complete studies of the progenitor evolution do not alter this picture (see, for example, Liu & Stancliffe 2017).

Narrow H α emission has been detected in a number of SNe Ia. In some events (e.g., SNe 2002ic or 2005gj), the detection is early, around bolometric maximum, and compatible with circumstellar-material (CSM) interaction (Hamuy et al. 2003; Silverman et al. 2013; Kotak et al. 2004). For two noteworthy

events, the H α emission has been detected later, at ~ 100 d past maximum or more (for example, SN 2018cuj, Prieto et al. 2020; ASASSN-18tb, Kollmeier et al. 2019; Vallely et al. 2019). These events may be explained by either CSM interaction (in particular when the detection occurs earlier, as for ASASSN-18tb at +39 d; Vallely et al. 2019) or by emission from stripped material from a companion. However, in the latter case, radiative transfer simulations, confirmed by the present work, suggest the stripped material mass M_{st} is on the order of $0.001 M_{\odot}$. This is much less than predicted by all hydrodynamical simulations of this scenario, which suggest that at least $0.1 M_{\odot}$ of material should be stripped (see original work by Marietta et al. 2000 and the most recent complete study by Liu et al. 2012). Another tension for the single-degenerate scenario is that such H α emission is very rarely seen (stringent upper limits on M_{st} are placed instead), even for the most nearby SN Ia events or those with very high quality observations (Leonard 2007; Lundqvist et al. 2013, 2015; Shappee et al. 2013, 2018; Maguire et al. 2016; Graham et al. 2017; Sand et al. 2018, 2019; Holmbo et al. 2019; Dimitriadis et al. 2019; Tucker et al. 2019, 2020), while theory predicts that it should instead be systematically detected. In the current framework, this is a major problem for the single-degenerate scenario for SNe Ia. One potential way out of the discrepancy may be to modify the donor star through some mechanism so that the amount of stripped, hydrogen-rich material is vastly reduced.

Such mechanisms could be hydrogen stripping by an optically thick wind so that it has a helium-rich envelope (Hachisu et al. 2008; Pan et al. 2010) or a “spin-up spin-down” phase that strips the envelope and also leaves a much more compact star (Justham 2011; Hachisu et al. 2012).

In this work, we focus on the emission properties that stripped material will have on the resulting spectrum. So far, only a few studies have been published on the non-local thermodynamic equilibrium (non-LTE) radiative-transfer modeling for SNe Ia with stripped material from a companion star. Mattila et al. (2005) and Lundqvist et al. (2013, 2015) use parametrized ejecta structures together with the radiative-transfer code of Kozma et al. (2005) to set constraints on the H α emission from the stripped material. Making a number of simplifications for the radiative transfer (Botyánszki & Kasen 2017), and in particular pure optically-thin line emission, Botyánszki et al. (2018) perform similar (i.e., Monte Carlo) simulations but based on physically consistent 3D hydrodynamical simulations of the ejecta–companion interaction. The study of Botyánszki et al. (2018) predicts H α luminosities that appear a hundred to a thousand times greater than those predicted by Mattila et al. (2005) for the same stripped material mass and composition. These various studies use the Sobolev approximation, and treat approximately, or ignore, line overlap and multiple scattering.

In this paper, we build on these previous studies and conduct non-LTE steady-state radiative transfer simulations for SNe Ia with stripped material for a range of post-explosion times, SN Ia ejecta (total mass and ^{56}Ni mass), as well as a large range of stripped material masses M_{st} . The simulations are performed with the standard setup for SN Ia calculations with CMFGEN (see, for example, Hillier & Dessart 2012; Dessart et al. 2014a; Wilk et al. 2020), treat all non-LTE processes, and employ a large model atom. The Sobolev approximation is not used, and line overlap and line blanketing are computed explicitly. This allows for an assessment of the blanketing effects of the metal-rich faster-moving ejecta on the emission from the stripped material, as well as all optical depth effects on continuum and line photons. As in Mattila et al. (2005), we adopt parametrized ejecta structures but also perform tests to evaluate the impact of this shortcoming on our results.

In the next section, we present our numerical approach. Section 3 studies in detail the results for a reference case, chosen to be a standard Chandrasekhar-mass SN Ia model (i.e., with $0.51 M_{\odot}$ of ^{56}Ni) with $0.18 M_{\odot}$ of stripped material. Section 4 elaborates on the processes that control the appearance of H α . Section 5 presents one clue for the identification of stripped material. Section 6 evaluates the limitations of our approach for the adopted structure of the stripped material. We also discuss the predicted signatures from He I lines in our simulations in Sect. 7. Section 8 presents results for the whole grid of simulations performed in this study, encompassing five epochs from 100 to 300 d, Chandrasekhar as well as sub-Chandrasekhar mass ejecta, ^{56}Ni masses from about 0.1 to $0.9 M_{\odot}$, and stripped material masses from 10^{-5} up to $0.5 M_{\odot}$. Section 9 emphasizes the distinction between line luminosity and line equivalent width and the relevance for the detection of H α from stripped material in SN Ia spectra. Section 10 presents our conclusions.

2. Numerical approach

We investigated the radiative signatures of stripped material in the innermost layers of SN Ia ejecta using a parametrized approach. For the SN Ia ejecta, rich in iron-group elements and H deficient, we adopted the 1D ejecta structure and composition

Table 1. Properties for the SN Ia ejecta used in this study.

Model	M_{ej} [M_{\odot}]	$M(^{56}\text{Ni})$ [M_{\odot}]
DDC0	1.41	0.86
DDC15	1.41	0.51
DDC25	1.41	0.12
SCH3p5	0.98	0.30

of the delayed-detonation models DDC0, DDC15, and DDC25 from Blondin et al. (2013). To test the influence of the ejecta mass, we also included the sub-Chandrasekhar mass model SCH3p5 from Blondin et al. (2017). In the same model order, the ^{56}Ni mass prior to any decay is 0.86, 0.51, 0.12, and $0.30 M_{\odot}$, and the ejecta mass is 1.41, 1.41, 1.41, and $0.98 M_{\odot}$ (Table 1). The simulations of Mattila et al. (2005) and Botyánszki et al. (2018), to which we will compare our results, are based on the pure-deflagration W7 model of Nomoto et al. (1984). This model is very similar to our model DDC15 below an ejecta velocity of about $10\,000 \text{ km s}^{-1}$ (see discussion in Blondin et al. 2015). Since this is the region that dominates the emission at nebular times, the relevant metal-rich part of our DDC15 model is analogous to that used in those two studies.

For the stripped material, we used a similar approach to Mattila et al. (2005) and prescribed a mass (in the range from $\sim 10^{-5}$ up to $\sim 0.5 M_{\odot}$) and defined the maximum velocity that limits its extension in space (typically 1000 km s^{-1}). We assumed homologous expansion for both regions so there is a direct correspondence between velocity V and radius R for a given SN age t through $R = Vt$. The case of a very low mass of stripped material (i.e., $10^{-5} M_{\odot}$) was used to gauge the impact of the stripped material in other models. Because these models have the same setup (grid, model atom, etc.), flux subtraction can be used to reveal subtle offsets associated with the emission from the stripped material. This helps, for example, to reveal a global but weak flux offset, or the putative presence of a weak H α line, in particular when it first appears.

To setup a model with stripped material, we took the SN Ia ejecta, cut out the inner regions below a chosen velocity limit (typically 1000 km s^{-1}) and replaced what used to be metal-rich material with some H-rich material with a metal composition at the solar value. We also reset the density in this inner region so that it varies as $1/V^2$ and yields the desired mass for the stripped material. The ejecta structure and composition of the SN Ia ejecta are left untouched above that velocity limit. To avoid sharp variations at this new interface, we applied a Gaussian smoothing to the density and composition. A representative ejecta structure resulting from this procedure is shown in Fig. 1 for the SN Ia model DDC15 with $0.18 M_{\odot}$ of stripped material. Other models varying in SN Ia ejecta composition (DDC0, DDC25), mass (SCH3p5), or in the mass of stripped material, have a similar structure but shifted up and down from the profiles shown in Fig. 1.

This setup is technically unphysical but operationally viable (see discussion in Sect. 6 where a comparison for two different stripped-material configurations is presented). The unphysical aspect arises since a real mass-stripping will yield material offset from the center of the explosion, asymmetrically distributed, and yielding line profiles whose width and centroid will be directionally dependent. This study remains worthwhile since the detectability at late times will not be affected by such considerations.

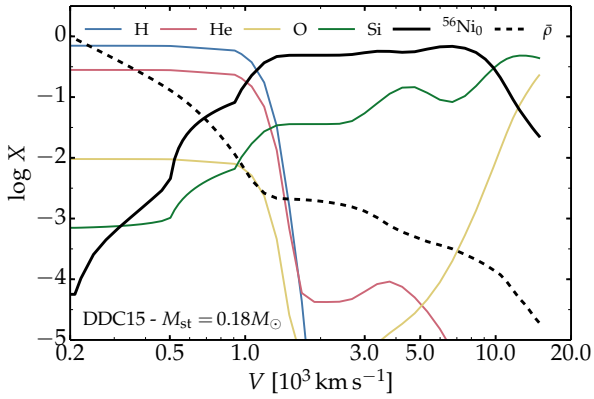


Fig. 1. Composition for a selection of elements and normalized density profile (dashed line) in the DDC15 model in which $0.18 M_{\odot}$ of H-rich stripped material has been introduced below 1000 km s^{-1} . The x -axis is shown in logarithmic space to better reveal the innermost regions and the junction between the stripped material (i.e., rich in H and He) and the SN Ia ejecta (i.e., rich in Si and ^{56}Ni).

For the radiative transfer, we used the same technique as described in our SN Ia calculations (see for example Dessart et al. 2014a). However, the model atom was extended to include H and He. We included the following metal species: C, O, Ne, Na, Mg, Al, Si, S, Ar, Ca, Sc, Ti, V, Cl, K, Cr, Mn, Fe, Co, and Ni. We included the following ions: H I, He I–II, C I–II, O I–II, Ne I–II, Na I, Mg II–III, Al II–III, Si II–III, S II–III, Ar I–III, Ca II–III, Sc II–III, Ti II–III, V I, Cl IV, K III, Cr II–IV, Mn II–III, Fe I–IV, Co II–IV, and Ni II–IV. The model atom used for all these atoms and ions is as described by Dessart & Hillier (2011) and in Appendix A of Dessart et al. (2014a). The large model atom was used for Co II and Co III. This implies that our calculations treat 1.66 million bound-bound transitions. We also included the same set of decay routes as in Dessart et al. (2014a) and described in Appendix B. Thus, we included the two-step decay chain of ^{56}Ni , as well as other two-step and one-step decay chains (see Dessart et al. 2014a for details and decay constants used). Unlike in Dessart et al. (2014a), wherein a Monte Carlo transport solver was used for the γ rays, we here employ a simple pure-absorption model (with $\kappa_{\gamma} = 0.06 Y_e \text{ cm}^2 \text{ g}^{-1}$, where Y_e is the electron fraction) for the computation of the γ -ray energy deposition (Swartz et al. 1995; Wilk et al. 2019).

Since we focus on late times, the very high velocity ejecta are optically thin. We thus reduced the maximum velocity of our grid to 15000 km s^{-1} . In contrast, the stripped material at low velocity is still very dense at 100–300 d for the larger values of M_{st} . This material has a continuum optical depth near unity, while Balmer lines remain optically thick, even at 300 d. The configurations explored here are thus distinct, from the point of view of the radiative transfer, from those of standard SNe Ia at a few hundred days. We will discuss these aspects in detail in the Results section below.

Unlike all previous simulations of SNe Ia with stripped material, which employ a Monte Carlo technique and use the Sobolev approximation, we treated the finite intrinsic width of lines and allowed for line overlap (Hillier & Miller 1998). We also introduced a turbulent velocity of 10 km s^{-1} . This value corresponds approximately to the thermal velocity of H atoms at 6000 K, but overestimates that of metals by a factor of a few. However, this is probably more physical for the radiative transfer (especially for H) than the zero intrinsic line width assumed in the Sobolev approximation.

Botyánszki et al. (2018) argued that some of the differences between their results and those of Mattila et al. (2005) stemmed from the higher physical consistency of their approach. There is more than a decade between these two studies, which differ in many ways other than the adopted hydrodynamical structure (one problem is that there is little detail on the radiative transfer and its limitations in either of these studies). Botyánszki et al. (2018) do not compare their results to an equivalent 1D setup. The asymmetric distribution of the stripped material causes a velocity shift of the $H\alpha$ line but it is not clear that it affects the total line flux, especially since they assume optically thin line formation. Furthermore, the hydrodynamical simulations of Botyánszki et al. (2018) predict $0.1\text{--}0.5 M_{\odot}$ of material stripped from the companion, as in previous studies. For lower masses of stripped material, their simulations are scaled-down versions and thus no longer physically consistent. It is not clear in this context that such adopted configurations are superior to the adopted ejecta of Mattila et al. (2005).

Although our work is based on parametrized 1D ejecta, we investigated the effect of a different distribution for the stripped material, by shifting it to larger velocities (outer bound at 2000 rather than 1000 km s^{-1} ; see Sect. 6). A relevant point to consider is what level of accuracy is needed to contribute to the current debate. Inferred masses of stripped material for ASASSN-18tb and SN2018cqj suggest very low values of about $0.001 M_{\odot}$ (Kollmeier et al. 2019; Prieto et al. 2020). Such low values are incompatible with the $0.1\text{--}0.5 M_{\odot}$ stripped material masses expected from the standard single-degenerate scenario for SNe Ia, and this holds whether one uses the model results of Mattila et al. (2005) or those of Botyánszki et al. (2018).

3. Study of the “standard” M_{ch} SN Ia model with stripped material

The left panel of Fig. 2 shows the results from our simulations for the DDC15 model, which is representative of a standard SN Ia with its ^{56}Ni mass of $0.51 M_{\odot}$ (other models are discussed in subsequent sections) with $M_{\text{st}} = 0.18 M_{\odot}$. The main signature associated with the stripped material is the narrow $H\alpha$ line. This is seen as a very weak feature at 100 d that progressively becomes the strongest line in the optical at 300 d, exceeding the strength of Fe III 4658 Å, which is produced by the outer, faster moving metal-rich ejecta. We will not make a comparison to this Fe III line in the rest of the paper because its strength varies with ^{56}Ni mass, the ionization level, clumping, and other factors, and it is thus not a robust physical probe. The $H\alpha$ line width never changes because the H-rich material is by design confined to the innermost regions, below about 1000 km s^{-1} . This is done to reflect the results from multi-D hydrodynamical simulations (Marietta et al. 2000). The luminosity decrease occurs at all wavelengths but more slowly for the $H\alpha$ line, which eventually becomes the strongest optical line.

The right panel of Fig. 2 shows the normalized flux for model DDC15 at 200 d but now for a range of stripped material masses covering from 0.0018 up to $0.58 M_{\odot}$. Qualitatively, the evolution with increasing M_{st} is similar to that in time for a fixed value of M_{st} : the $H\alpha$ line strengthens relative to the rest of the spectrum. However, the changes are now roughly at constant luminosity so only the $H\alpha$ line changes with varying M_{st} (this is the reason for plotting the normalized flux). The luminosity is only roughly constant because at a given time a greater decay power is absorbed for increasing stripped material mass (see Sect. 8.2).

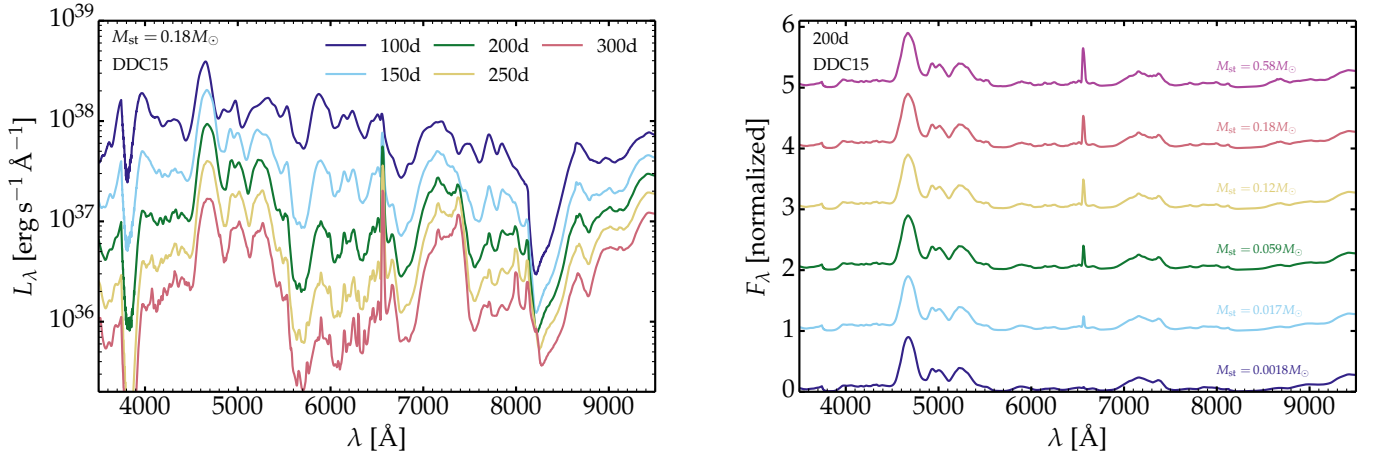


Fig. 2. *Left:* multi-epoch spectra (at 100, 150, 200, 250, and 300 d after explosion) for the SN Ia model DDC15 with a stripped-material mass M_{st} of $0.18 M_{\odot}$. *Right:* same as left, but for the model DDC15 at 200 d and for a range of stripped material mass of 0.0018, 0.017, 0.059, 0.12, 0.18, and $0.58 M_{\odot}$. In a qualitative sense, time and M_{st} have a similar impact on the optical spectrum, with a strengthening of the $H\alpha$ line relative to other spectral features with either time or M_{st} . Quantitatively, the correspondence does not hold since the bolometric luminosity changes significantly with time but only weakly with M_{st} at a given time.

The physical interpretation for these results has been discussed in the past (Mattila et al. 2005; Botyánszki et al. 2018), although results for multiple epochs have not been shown before. The power source is ^{56}Co decay. Of the total decay power absorbed, positrons (whose energy is assumed to be deposited locally) contribute 15% at 100 d and this contribution grows roughly linearly in time to 53% at 300 d. However, this positron contribution exclusively benefits the metal-rich ejecta, from which the γ -rays escape increasingly with time. For the stripped material, the situation is very different. Being free of ^{56}Ni (and ^{56}Co), it can only be powered by the non-local deposition of γ -ray energy, which is not negligible because of the high density of this H-rich material (this efficiency is also boosted because the opacity to γ -rays is greater for H-rich material owing to its larger electron fraction, which is about 0.8 rather than 0.5 for symmetric nuclear matter). So, as time passes from 100 to 300 d, the metal-rich ejecta receive a decreasing fraction of the total decay power absorbed, leading to a relative strengthening of the emission from the stripped material and in particular $H\alpha$ (we find that this line radiates typically 10% of the decay power absorbed by the stripped material; see Sect. 8.2). For an increased stripped material mass (see example in the right panel of Fig. 2), more decay power is absorbed and the $H\alpha$ line flux increases relative to the emission from the metal-rich ejecta.

At 200 d for model DDC15, $H\alpha$ is seen unambiguously for M_{st} greater than about $0.01 M_{\odot}$, and is essentially impossible to detect for M_{st} below $0.001 M_{\odot}$. An important property of this stripped material is that if $H\alpha$ can be detected around 100 d, it should be detected for months thereafter since its relative strength to metal lines like Fe III 4658 Å grows in time. A disappearance at late times is not expected in the context of stripped material from a non-degenerate companion. It could be caused by an insufficient decay power absorbed by the stripped material, as may occur if M_{st} were low or very low, but this should compromise the $H\alpha$ detectability at early times as well.

Figure 3 shows how the different ejecta regions (indicated here in velocity space) contribute to the emergent luminosity (or flux) at a given wavelength. This illustration is exact in the sense that the sum of the flux contributions at a given wavelength give the total emergent flux at that wavelength. The stripped material contributes through the strong $H\alpha$ line, as well as some weak

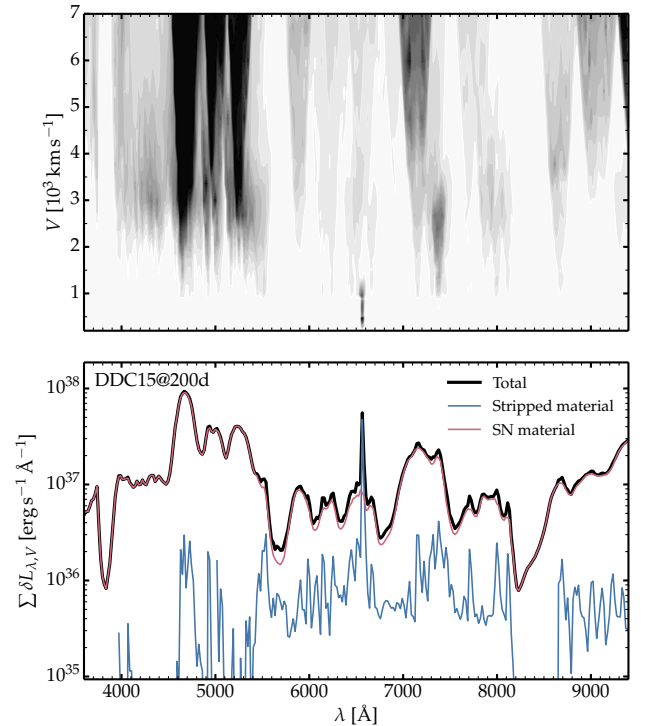


Fig. 3. Illustration of the ejecta regions (in velocity space) at the origin of the optical flux for model DDC15 with $M_{\text{st}} = 0.18 M_{\odot}$ at 200 d. The *top panel* shows a gray linear scale of the (emergent) luminosity $\delta L_{\lambda, V}$ while the *bottom panel* shows the contributions (ordinate in logarithmic space) for the full ejecta and those from the stripped material (blue) or the metal-rich ejecta (red). As is evident from these plots, the predominant emerging feature due to stripped material of the companion star at optical wavelengths is $H\alpha$.

and narrow metal lines. The continuum flux is so weak that even weak lines supersede it, with the exception of the spectral region around 6700–7000 Å (see also Chugai 1986). The metal-line emission from the ejecta appears as broad and strong lines (mostly from Fe II, Fe III, and Ca II). For Ca II 7300 Å and some Fe II lines, there is both a broad component from the metal-rich

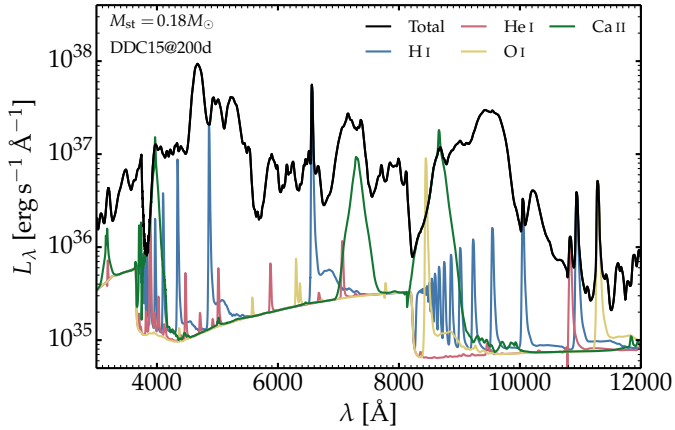


Fig. 4. Synthetic spectra for the SN Ia model DDC15 with $0.18 M_{\odot}$ of stripped material. We show the total emergent luminosity L_{λ} as well as that associated with the continuum and bound-bound transition of selected ions (H I, He I, O I, and Ca II). The calculations for the latter are done by assuming that only the selected ion contributes (together with all continuum processes) and thus ignore the impact of other ions on that selected ion (such as metal-line blanketing on the H I lines arising from the innermost regions associated with the stripped material). The other three models show a similar behavior to that shown here for model DDC15. Hence, while the stripped, low-velocity material is expected to radiate quite strongly at many wavelengths, the primary observable feature at optical wavelengths is due to $H\alpha$.

ejecta and a narrow component from the H-rich stripped material (in which all metal mass fractions are at the solar value).

Figure 4 gives a complementary perspective to that of Fig. 3. It shows the flux that a given ion would produce in the absence of other ions. This is more artificial than the information presented in Fig. 3 because it ignores any cross-talk between ions, line overlap, and related optical depth effects. By identifying the differences between the full spectrum and the intrinsic contribution of each ion, however, one can assess the importance of optical depth effects (suggested early on by Chugai 1986 and later by Leonard 2007). These optical depth effects are unambiguously present since the individual ion spectra are rich in many narrow lines, yet none but $H\alpha$ is obviously seen in the total optical flux. The continuum level is 10–100 times weaker than the total flux in the emergent spectrum, with an offset that decreases towards longer optical wavelengths.

Some lines suffer from overlap with strong line emission from the metal-rich fast moving ejecta. This strong brightness contrast compromises the identification of the contribution from the stripped material. Other lines suffer from strong attenuation by the metal rich regions, like $H\beta$. In that case, the metal-rich ejecta act as a “curtain” that blocks the incoming radiation from the inner regions, as suggested by Leonard (2007). In terms of detectability in the emergent spectrum, the lines of interest sit in regions of lower opacity, and include $H\alpha$, He I $1.083 \mu\text{m}$, H I $1.093 \mu\text{m}$, and O I $1.129 \mu\text{m}$ and thus appear as strong narrow features. The resulting emission in the total emergent spectrum is roughly the sum of the individual contributions at the corresponding wavelength. The appearance of narrow lines is in part fortuitous because it arises from the non-uniform distribution of line opacity with wavelength. Overall, the region below 5000 \AA remains thick until late times because of metal-line blanketing, even though the continuum optical depth of these regions is negligible. Consequently, lines like $H\beta$ are attenuated persistently.

Such optical depth effects – and the associated absence of line features in the resulting spectrum – have not been treated or discussed by prior studies since strong, narrow features are seen in the predicted synthetic spectrum (see, for example, Botyánszki et al. 2018). This may lead to artificially restrictive limits on the stripped material based on the non-existence of these lines in the observed spectrum (e.g., Tucker et al. 2020).

We note that there are weak bumps on the red side of the strongest lines in the individual ion spectrum calculations (see, for example, the blue curve for H I lines in Fig. 4). The electron scattering optical depth is below, but close to, unity for the metal-rich ejecta, and this is enough to cause one scattering with a free electron at a large velocity of many thousands of kilometers per second. The associated redshift yields an excess flux between about $10\,000$ and $20\,000 \text{ km s}^{-1}$ on the red side of the lines. This is compatible with the ejecta kinematics. The effect cannot be caused by other lines since the $H\beta$ and $H\alpha$ profiles can be overlaid nearly exactly (after a flux scaling). These bumps weaken and move to lower velocities (toward line center) with increasing time, being nearly absent at 300 d. All these properties are compatible with an electron-scattering origin.

4. Appearance of $H\alpha$ and optical depth effects

In the simulation DDC15 with $M_{\text{st}} = 0.18 M_{\odot}$ presented above, the $H\alpha$ line grows from being very weak relative to the rest of the spectrum at 100 d to becoming the strongest line (in terms of peak flux rather than line flux or equivalent width; see Sect. 9) in the optical at 300 d. This is shown more clearly in Fig. 5 where we isolate the $H\alpha$ region. When inspecting the luminosity (top row), $H\alpha$ is a small bump at 100 d. Its luminosity is very large but so is that of the metal-rich ejecta so the contrast between $H\alpha$ and the overlapping Fe II lines is small. To better reveal the presence of $H\alpha$, we plot in the bottom row the difference in luminosity between a given model and its counterpart in which $M_{\text{st}} = 10^{-5} M_{\odot}$. The $H\alpha$ line is then unambiguously seen, even for $M_{\text{st}} = 0.0018 M_{\odot}$.

At early times, the small luminosity contrast between metal-rich regions and the stripped material is one limitation to identifying $H\alpha$. At such times, the γ -ray escape from the metal-rich regions is moderate so these regions outshine the inner H-rich ejecta. The contribution is more extended so both the regions rich in iron-group and intermediate-mass elements contribute, which leads to a more widespread presence of lines in the optical. With time, the metal-rich region traps less decay power, and the emission is biased inward in favor of the iron-rich regions, so holes appear in the continuum-free spectrum.

The other limitation is optical depth. There are contributions, of different magnitudes, from electron scattering and lines, and from the metal-rich SN Ia ejecta as well as from the H-rich stripped material. Figure 6 shows the evolution of the electron-scattering and Rosseland mean optical depth at 1000, 2000, and 3000 km s^{-1} in the SN Ia ejecta of model DDC15 from 30 to 100 d after explosion¹. Because of the significant impact of lines, the latter is well above the former, although one needs to bear in mind that the Rosseland mean is not an ideal representation of opacity in optically thin regions. Nonetheless,

¹ We use here the time sequence for model DDC15 (Dessart et al. 2014b), which ignores any stripped material from a non-degenerate companion. Since we focus on the optical depth of the SN Ia ejecta overlying the putative stripped material located below 1000 km s^{-1} , these simulations are suitable for estimating the optical depth of the metal-rich ejecta in the time range 30–100 d.

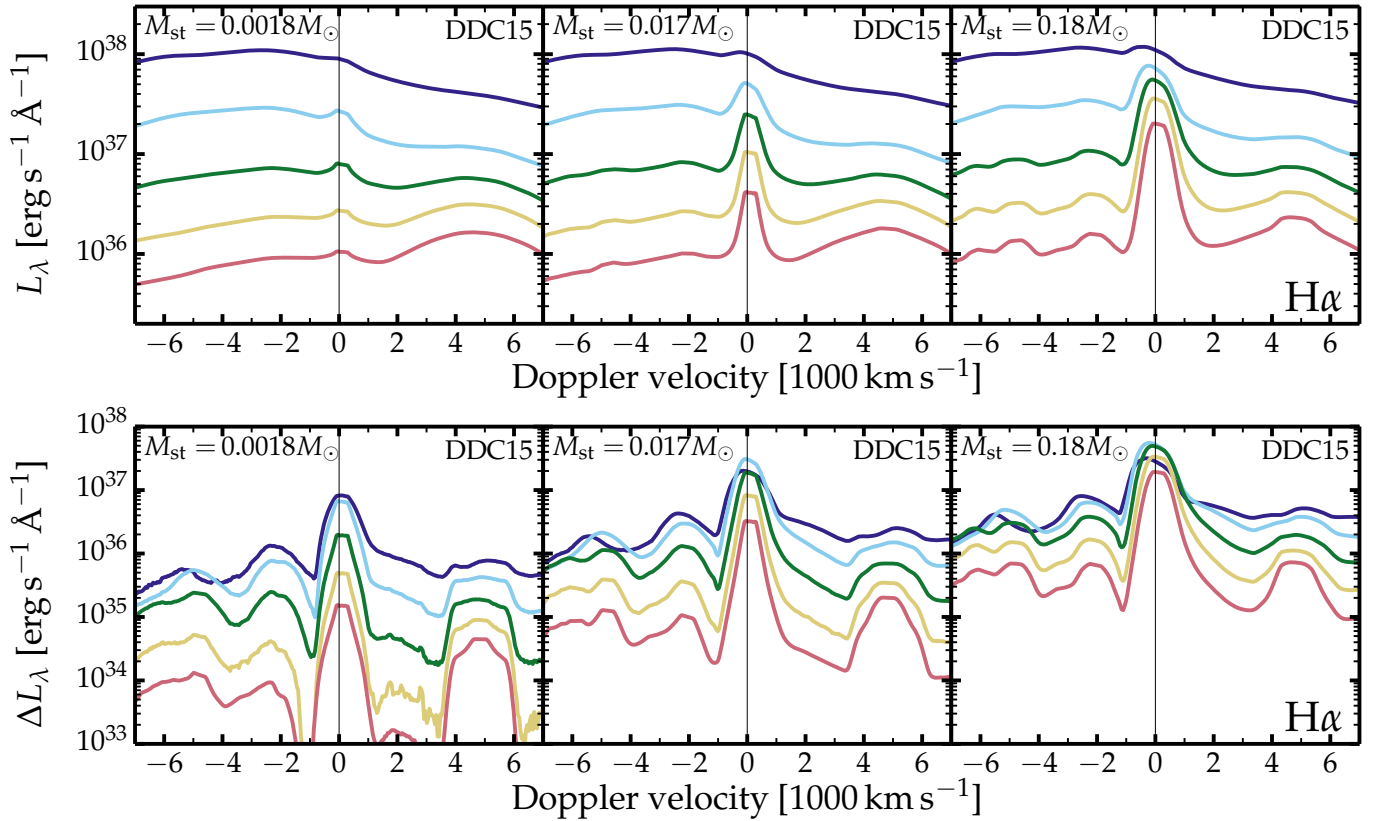


Fig. 5. *Top:* emergent luminosity in the H α region and multiple epochs for model DDC15 with M_{st} of 0.0018, 0.017, and $0.18 M_{\odot}$ from left to right. The color coding indicates epochs 100, 150, 200, 250, and 300 d after explosion (time increases from the upper curve to the lower curve; see also left panel of Fig. 2). *Bottom:* same as top, but we now subtract the luminosity arising from the model with $M_{\text{st}} = 10^{-5} M_{\odot}$, which has the effect of erasing the luminosity contribution from the metal-rich, SN Ia ejecta. The stripped material contributes not just through H α emission, but also weak emission from other lines (e.g., Fe II) and some weak background continuum.

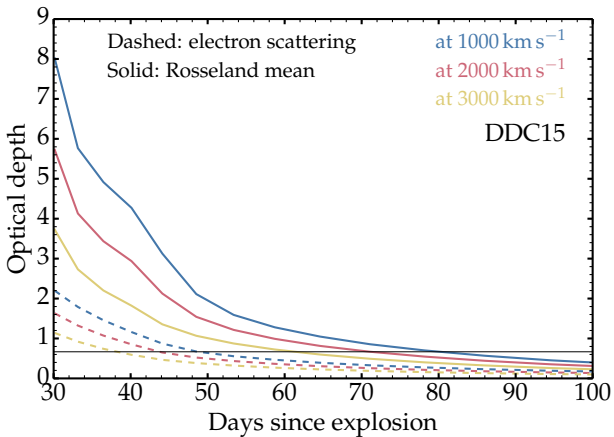


Fig. 6. Evolution of the Rosseland-mean (solid) and electron scattering (dashed) optical depth down to the ejecta regions at 1000, 2000, and 3000 km s^{-1} for model DDC15 and shown between 30 and 100 d after explosion. The optical depth of $2/3$ representing the “photosphere” is shown as a thin black line.

one sees that the conditions are only moderately optically thin even at 100 d and that they are optically thick at 50 d. Because of expansion, electron scattering redistributes the line flux but does not destroy photons, so this may not quench line emission from the inner stripped material. Metal-line blanketing is in part absorptive but the non-uniform distribution of lines implies that

even for optically thick conditions according to the Rosseland mean, some spectral regions may remain opacity holes. This is reflected by the strong variation of the photospheric velocity with wavelength and time (Fig. 7). One should bear in mind that the photosphere is not an opaque wall below which no photons escape. Instead, it represents the layer of “median” emission, in other words about 50% of the emerging photons come from below that layer and the rest from above. So, “opaque” regions (i.e., those located at an optical depth greater than unity) do contribute to the emergent radiation. Hence, Fig. 7 is merely illustrative of the non-uniform trapping efficiency through the optical range.

Figure 6 does not show the opacity associated with the stripped material itself. For model DDC15 with $M_{\text{st}} = 0.18 M_{\odot}$, the Rosseland-mean (electron-scattering) optical depth at the base of the ejecta (considering the whole column of material above the innermost ejecta layer at 200 km s^{-1}) drops from 3.4 to 0.22 (from 2.54 to 0.17) between 100 and 300 d. This is a greater reduction than expected for homologous expansion (wherein $\tau \propto 1/t^2$) because of a simultaneous reduction in ionization. This dependence on ionization level usually applies when electron scattering dominates, but in some cases opacity can rise with decreasing ionization if this shift leads to a greater supply of optically thick lines.

An additional ingredient is the optical depth of the line itself (its intrinsic optical depth). The stripped material is quite abundant (representing up to a third of the SN Ia ejecta mass, for example, if we consider M_{st} of $0.5 M_{\odot}$) and is also located at the

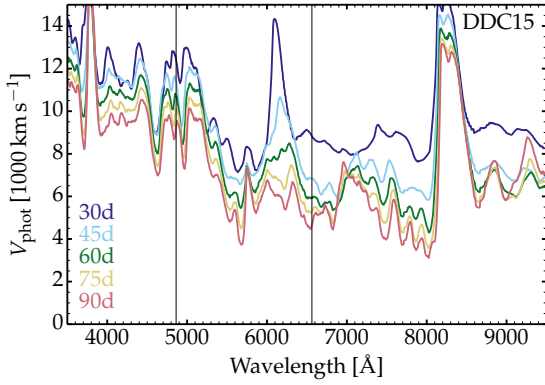


Fig. 7. Evolution of the photospheric velocity from 30 to 90 d after explosion in model DDC15. The two vertical lines give the location of $H\alpha$ and $H\beta$. This computation includes the effects of all opacity sources and is thus more relevant than the Rosseland-mean (because not very physical at low optical depth) or the electron-scattering (because it strongly underestimates the true opacity) optical depth shown in Fig. 6. This figure shows that $H\beta$ sits in a region of strong blanketing (since photons essentially decouple at 9000–12 000 km s^{-1} at the times depicted) while $H\alpha$ sits in one of the most transparent regions of the optical range.

lowest velocities, hence the highest densities. For model DDC15 with $M_{\text{st}} = 0.18 M_{\odot}$, we find that $H\alpha$ has an optical depth of 100 or more in its formation region over the period 100–300 d. The $H\alpha$ optical depth becomes small in regions where the H mass fraction is small or negligible (thus contributing no emission). Hence, $H\alpha$ is optically thick at all times (even if M_{st} is reduced by a factor of 100). The same holds but to a smaller degree for $H\beta$. This implies that optically thin line formation for Balmer lines is not a valid assumption. This may be one origin for the differences in the results of Mattila et al. (2005) and those of Botyánszki et al. (2018).

To conclude, our simulations of stripped material in SN Ia ejecta suggest that the $H\alpha$ line (and emission from the stripped material) suffers from a brightness contrast with the metal-rich ejecta as well as optical depth effects that are both intrinsic and extrinsic. As a consequence, the $H\alpha$ line, which is the strongest signature from the stripped material, is essentially impossible to detect prior to 50 d (metal-rich ejecta are optically thick and too luminous), hard to detect at 100 d (metal-rich ejecta are not as optically thick but still very luminous) but increasingly strong as time progresses (metal-rich ejecta become increasingly transparent and faint). The easiest line to detect is $H\alpha$ in part because it lies in a region largely devoid of strong or optically thick metal lines.

Optical depth effects also cause a blueshift of line profiles, which is most obviously seen through the location of peak flux in the line. This effect is well understood (Dessart & Hillier 2005) and routinely observed in a variety of SNe (Blondin et al. 2006; Anderson et al. 2014; Zhang et al. 2012). Here, the effect is present over the period 100–200 d after explosion (see Fig. 5 and the next section) for cases in which M_{st} is greater than about $0.1 M_{\odot}$. Hence, line shifts may not result exclusively from an asymmetric ejecta. This complicates the identification of multidimensional effects (Botyánszki et al. 2018).

5. Conclusive evidence for the identification of stripped material

A concern from the observations of $H\alpha$ in SNe Ia at 100–300 d after explosion is whether the emission arises from the presence

of stripped material in the innermost ejecta layers (the context explored here) or whether the emission is external to the ejecta and arises from interaction with the H-rich CSM (produced by wind mass loss and mass transfer in the progenitor system). The results described above provide some clues to this problem.

Figure 8 presents the evolution of the $H\beta$ and $H\alpha$ regions at 100, 150, 200, 250, and 300 d after explosion in the model DDC15 with $M_{\text{st}} = 0.18 M_{\odot}$. The total flux (thick black curve) is shown together with the predictions of the model counterpart with $M_{\text{st}} = 10^{-5} M_{\odot}$ (thin black curve). If we subtract the two, we can see the contribution from $H\beta$ and $H\alpha$ as a function of time in the model with $0.18 M_{\odot}$ of stripped material (thick red line). The contribution to $H\alpha$ is significant at all times, and represents the total strength of the feature at 6562 Å at 300 d since it coincides with the total flux. For $H\beta$, the line is absent until 200 d and only rises as a very weak feature at 250–300 d. The presence of $H\alpha$ and the absence of $H\beta$ is caused by metal-line blanketing. If we compute the H I spectrum by ignoring all other ions (and associated emission and absorption), we see that both $H\alpha$ and $H\beta$ are present (thick red dashed line). In each case, the line also peaks blueward of its rest wavelength up until 200 d, indicating that it forms under optically thick conditions.

The strong metal-line blanketing by the metal-rich ejecta thus offers a clear indication of the presence of stripped material since in that case only $H\alpha$ should be seen. $H\beta$ photons are destroyed by metal lines at all times prior to about 300 d and should not be seen if the emission arises from stripped material at low velocity. Hence, the detection of $H\beta$ in SNe Ia suggests that the emission arises from regions outside the SN Ia ejecta, free of metal-line blanketing, and thus most likely arising from interaction with CSM. High signal to noise ratio (S/N) observations of the optical and in particular the $H\beta$ region are essential to distinguish both scenarios.

6. Influence of the adopted stripped material velocity and density

In our simulations, we assumed spherical symmetry and adopted a centrally concentrated distribution for the stripped material. The outer bound of this region is around 1000 km s^{-1} . Multidimensional hydrodynamical simulations suggest that the stripped material can be offset to larger velocities, as well as offset from the ejecta center (Marietta et al. 2000; Pakmor et al. 2008; Liu et al. 2012; Pan et al. 2012; Botyánszki et al. 2018). To test this effect, we recomputed model DDC15 with $M_{\text{st}} = 0.18 M_{\odot}$ but using a distribution of stripped material centered around (rather than bounded by) 1000 km s^{-1} , extending from 200 km s^{-1} up to about 2000 km s^{-1} . The stripped material is now a hollow shell, occupying a larger volume, but still symmetric around the ejecta center. The Gaussian smoothing does not conserve the mass exactly in the innermost layers (because of the density profile at the inner boundary) so the stripped material mass is 30% lower in the “offset” model.

Figure 9 shows the impact of the stripped material distribution on the ejecta properties. With the offset, the stripped material is shifted to larger velocities, corresponding to lower densities (aggravated by the 30% lower stripped material mass). The electron density shows a broader bump for this H-rich material, with a slightly higher temperature, and a higher mean ionization for H (same ionization for He). The decay power absorbed by the stripped material is comparable in both models.

However, the $H\alpha$ line in the “offset” model is twice as strong in total line flux and 30% stronger in peak flux (Fig. 10). The $H\alpha$

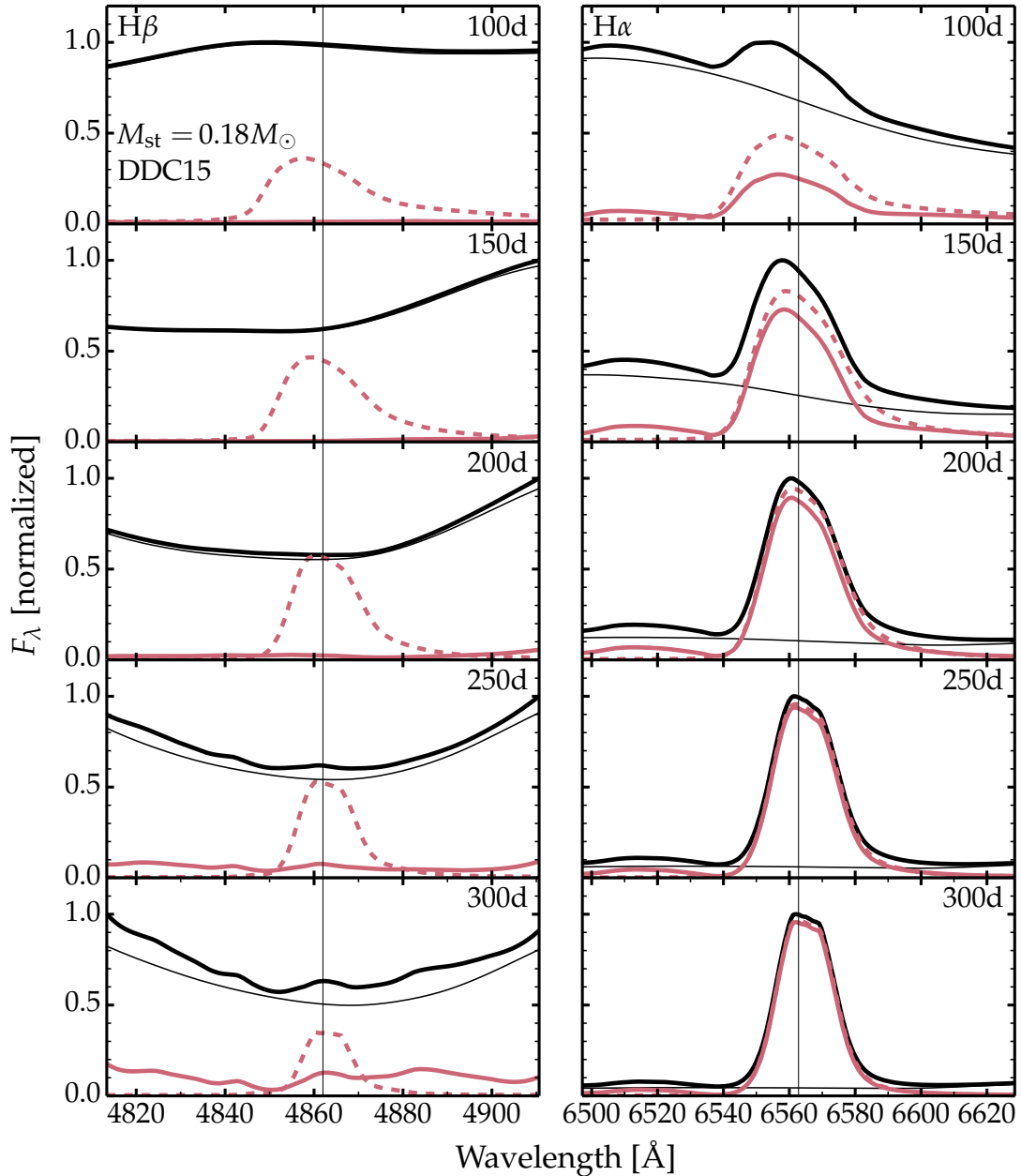


Fig. 8. Comparison of the spectral regions around $H\beta$ (left) and $H\alpha$ (right) for model DDC15 with $M_{\text{st}} = 0.18 M_{\odot}$ (thick black curve) and $M_{\text{st}} = 10^{-5} M_{\odot}$ (thin black curve; the stripped material contributes negligibly in that case). The different epochs spanning 100 to 300 d are stacked vertically. The difference between the two models gives a physical measure of the contribution from the stripped material (thick red line). For comparison, we show the H I spectrum that results if we neglect the influence of all other ions (thick dashed red line). It can thus be used to gauge the influence of the metal-rich ejecta on the emission from the stripped material. This influence is moderate or negligible for $H\alpha$, but very strong for $H\beta$. This figure shows that stripped material is not expected to yield any observable $H\beta$ emission for hundreds of days because of metal-line blanketing from the metal-rich (SN Ia) ejecta, whereas $H\alpha$ emission is prominent.

line is also broader because of its formation at higher velocities. The change in strength likely arises from a formation at lower optical depth, both in the continuum and in the line. The formation over a larger volume probably contributes to desaturate the line since $H\alpha$ photons are emitted over a broader range of velocities.

The choice of parametrized configurations that we use here, in the spirit of Mattila et al. (2005), can itself lead to significant variations in $H\alpha$ line strength, so this needs to be borne in mind when estimating the stripped material mass from observations. The factor of two found here, however, is much smaller

than the difference between predicted values for M_{st} in the single-degenerate scenario and the inferred values for M_{st} from observations.

7. He I lines

He I lines are non-thermally excited in our simulations and are predicted to be present but weak in the He I-only spectra that we compute (Fig. 4). In the total emergent spectrum, the weak feature at 5900 Å is due to Na I D, while He I 5875 Å is absent (left panel of Fig. 11). The only unambiguous He signature is

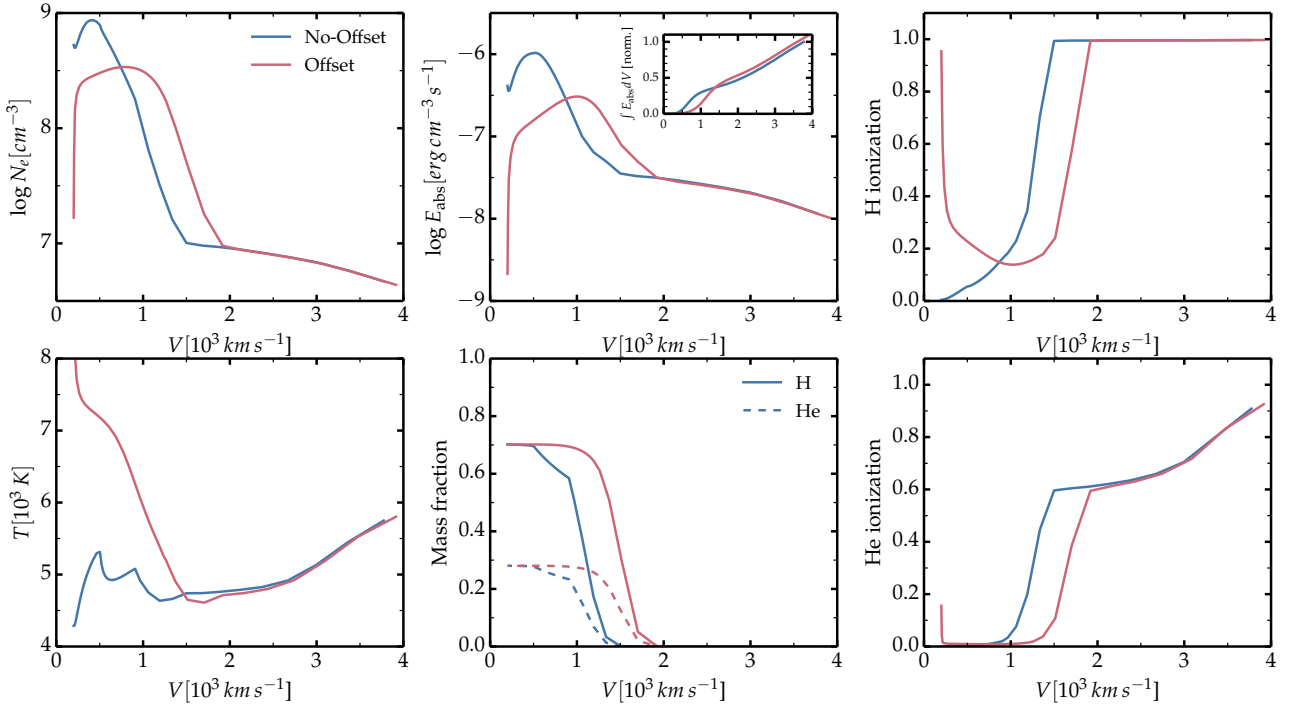


Fig. 9. Impact of the adopted density profile for the stripped material on the gas properties in model DDC15. This model has a M_{st} of about $0.15 M_{\odot}$ (the value is 30% lower in the model with offset) and at a SN age of 200 d. The simulations are 1D (i.e., assume spherical symmetry), but the simulation “No-offset” uses a more centrally concentrated mass distribution than the simulation “Offset” (see the electron-density profile, which reflects closely the difference in mass density profile). In the inset of the *top-middle panel*, the normalization of the cumulative decay power absorbed is set to the value obtained for the model with no offset (and limited to the velocity region shown).

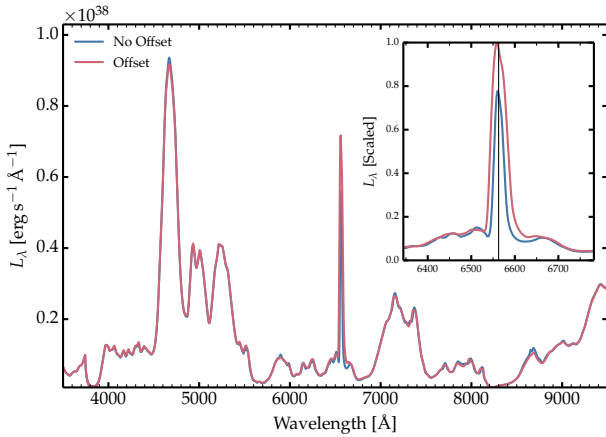


Fig. 10. Same as Fig. 9, but now showing the impact of the adopted density profile for the stripped material on the optical radiation.

He I 10830 Å in the near infrared (right panel of Fig. 11) because this line is usually the strongest under similar SN ejecta conditions (Li et al. 2012). Metal-line blanketing is also weaker in the near infrared and the stripped material is only a few times fainter than the metal-rich ejecta in this spectral region. The He I 10830 Å line is not affected by metal-line blanketing even at 100 d after explosion (this holds because the solid and dashed lines essentially overlap; see Fig. 8 for explanations).

This result is not surprising since the properties of the stripped material in a SN Ia ejecta at such late times are analogous to those found in Type II SN ejecta at the same epoch. In general, He I lines are not observed or predicted in optical spectra of type II SNe at nebular times (see, for example, Silverman et al.

2017; Jerkstrand et al. 2012; the models of Dessart et al. (2013) predict the presence of He I 7065 Å and overestimate its strength, but the problem is caused by the adoption of a high turbulent velocity not used here; Dessart & Hillier, in prep.).

Our results disagree with the predictions of Botyánszki et al. (2018). This may arise from their neglect of optical depth effects (especially in the optical). We also find that a significant power absorbed by the stripped material emerges in the continuum (or in lines that are later reprocessed by the metal rich ejecta), while they seem to assume that the gas can only cool through (optically thin) line emission.

8. Results for the grid of models

We now turn to the presentation of results for the whole grid of simulations. We have performed radiative transfer calculations at 100, 150, 200, 250, and 300 d for models DDC0 (^{56}Ni mass is $0.86 M_{\odot}$), DDC15 (^{56}Ni mass is $0.51 M_{\odot}$), DDC25 (^{56}Ni mass is $0.12 M_{\odot}$), and SCH3p5 (^{56}Ni mass is $0.30 M_{\odot}$) and stripped material masses of 0.0018 , 0.018 , and $0.18 M_{\odot}$. For each SN Ia model and epoch, we also computed the cases of a very low stripped material mass of $10^{-5} M_{\odot}$ to facilitate the assessment of the contribution of the stripped material when its influence is weak. For models DDC0, DDC15, and DDC25, additional simulations were also done to better cover the region around $M_{\text{st}} = 0.1 M_{\odot}$. In total, the grid comprises more than a hundred simulations and encompasses a much wider range of values in ^{56}Ni mass and M_{st} than studied so far.

8.1. $H\alpha$ luminosity and comparison to observations

Figure 12 shows the $H\alpha$ luminosity versus stripped material mass for all SN Ia ejecta models (symbols) and epochs (color coding);

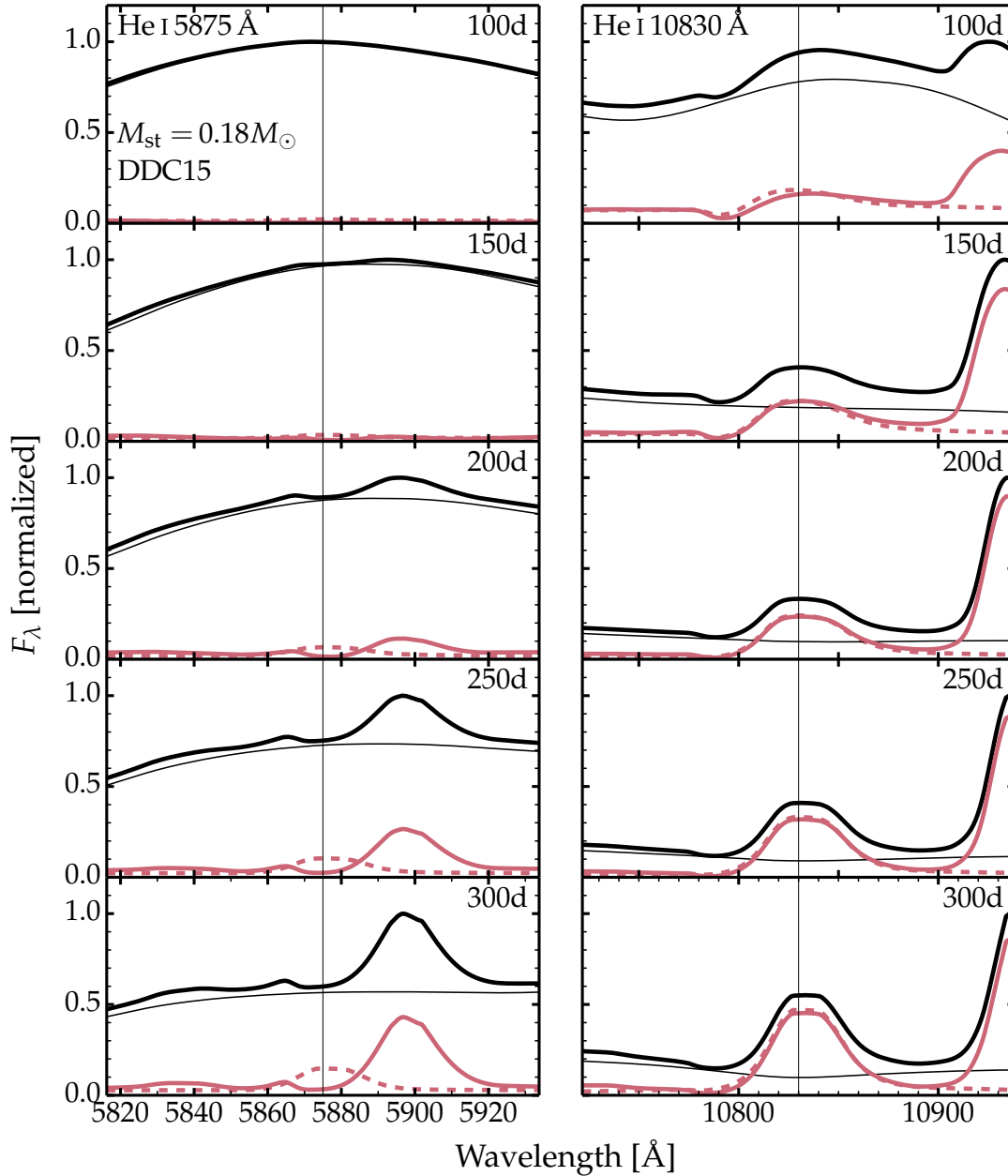


Fig. 11. Same as Fig. 8, but for the spectral regions centered on He I 5875 Å (*left*) and He I 10830 Å (*right*). He I 5875 Å is absent in the total emergent spectrum, and at best weak at late times in the He I-only spectrum. The only weak feature we predict is Na I D. He I 10830 Å is present at all times, is strong, and largely unaffected by the metal-rich ejecta (in either emission or absorption).

polynomial fits to the model results are provided in Appendix A. Two different ways are used to compute the $H\alpha$ luminosity. For the top panel, we computed the H I spectrum and integrated over $H\alpha$ to obtain the corresponding line flux and luminosity. For the bottom panel, we computed the total emergent spectrum and subtracted the spectrum for the model counterpart with $M_{\text{st}} = 10^{-5} M_{\odot}$. The two methods differ by up to a factor of two at times prior to 200 d (Sect. 5 and Fig. 8).

Computed either way, the $H\alpha$ luminosity reaches a maximum of a few 10^{39} erg s^{-1} at 100 d for the largest values of M_{st} . This luminosity tends to drop as time progresses (although in a complicated way; see below) or with stripped material mass. Variations in ^{56}Ni mass between models lead to similar variations in $H\alpha$ luminosity. The general pattern shown in log-log space does not allow a fine assessment. However, it is clear that

the inferred $H\alpha$ line luminosities by Kollmeier et al. (2019) and Prieto et al. (2020) for ASASSN-18tb and SN 2018cqj are both compatible with our models with M_{st} of about $0.002 M_{\odot}$, which is in agreement with their analysis.

Our $H\alpha$ luminosities are lower by a factor of five to ten than those of Botyánszki et al. (2018), which are given at a SN age of 200 d (green solid line in Fig. 12). This offset probably stems in part from the differences in the hydrodynamical structure of the ejecta, since their computed ejecta configurations tend to have the stripped material offset at a higher velocity than adopted in our work (see results and discussion in Sect. 6). It is likely that differences also result from optical depth effects (Sect. 4), or differences in the model atom and metal composition for the stripped material (metals can play an important part in the cooling of the gas even at low abundance).

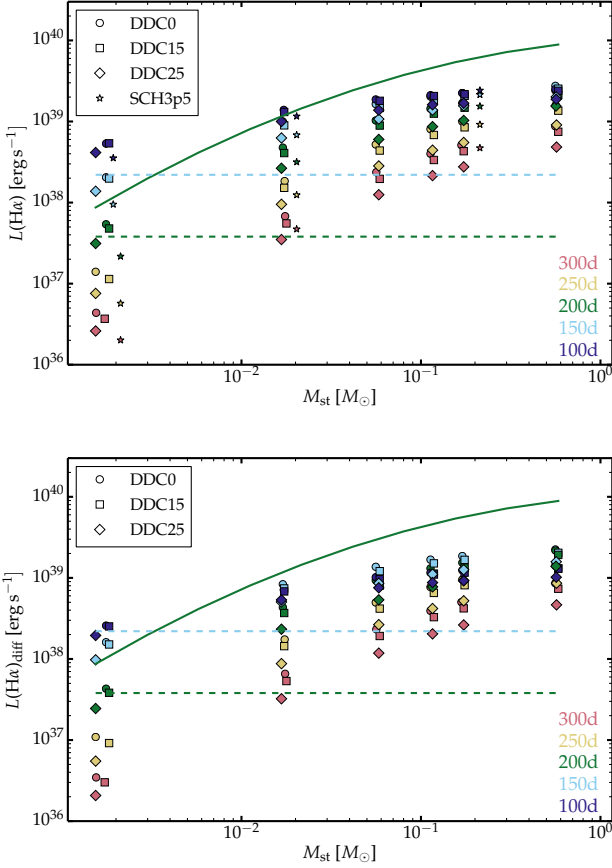


Fig. 12. *Top:* variation of the $H\alpha$ luminosity as a function of the adopted stripped-material mass M_{st} for our set of M_{ch} delayed-detonation simulations DDC0 (^{56}Ni mass is $0.86 M_{\odot}$), DDC15 (^{56}Ni mass is $0.51 M_{\odot}$), DDC25 (^{56}Ni mass is $0.12 M_{\odot}$), and sub- M_{ch} detonation model SCH3p5 (^{56}Ni mass is $0.30 M_{\odot}$). The calculation is based on the H I spectrum computed by neglecting all other ions and thus ignores blanketing effects from the metal-rich ejecta. The color coding defines the SN age, from 100 to 300 d after explosion. The solid (green) curve corresponds to the calibration of Botyánszki et al. (2018) based on their model calculations (and corrected for the typo in their Eq. (1)). The dashed lines correspond to the observed $H\alpha$ luminosity in ASASSN-18tb at ~ 153 d (Kollmeier et al. 2019; dashed line drawn in turquoise to match the color used for models computed at 150 d) and SN 2018cuj at ~ 207 d (Prieto et al. 2020; dashed line drawn in green to match the color used for models computed at 200 d), compatible with our models that have a stripped-material mass of about $0.002 M_{\odot}$. *Bottom:* same as top (with the omission of results for SCH3p5 models), but we compute the $H\alpha$ luminosity as given by subtracting the model with no stripped material (i.e., the model with $M_{\text{st}} = 10^{-5} M_{\odot}$) from the model with the stripped material. This yields a lower $H\alpha$ luminosity by up to a factor of two at times prior to 200 d, but makes little difference later on (see Fig. 8 and discussion in Sect. 5).

8.2. $H\alpha$ luminosity versus decay power absorbed

We find that the $H\alpha$ line radiates about 10% (extending from 5% up to 30% for a few outliers) of the decay power absorbed by the stripped material (Fig. 13), with no clear dependence with SN age, M_{st} , or ^{56}Ni mass. In particular, this fraction stays about constant despite the large variations in decay power absorbed with SN age and with M_{st} (Fig. 14).

Here, we quote the $H\alpha$ flux from an H I spectrum calculation, thus without any influence from the metal-rich ejecta. By doing this, we can gauge the cooling power of $H\alpha$ for the stripped material. This implies that 90% of the decay power absorbed

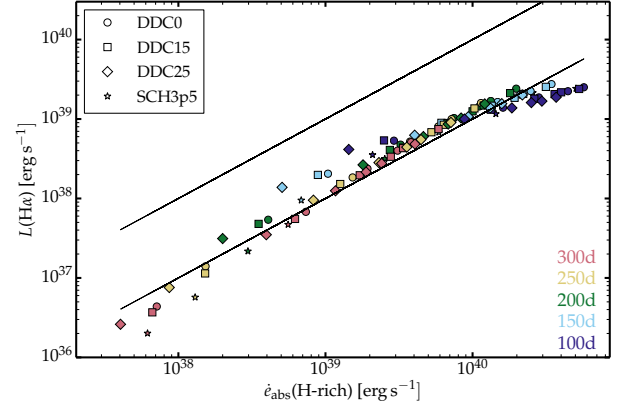


Fig. 13. $H\alpha$ luminosity $L(H\alpha)$ vs. decay power absorbed by the H-rich stripped material from the companion. The two black lines correspond to the cases where $L(H\alpha) = \dot{\epsilon}_{\text{abs}}(\text{H-rich})$ and $L(H\alpha) = 0.1 \dot{\epsilon}_{\text{abs}}(\text{H-rich})$. For most models, $H\alpha$ radiates about 10% (the distribution covers from 5 to 30% due to several outliers, all for a low stripped material mass) of the decay power absorbed by the stripped material (this material is ^{56}Ni deficient and thus the power stems from non-local γ -ray energy deposition).

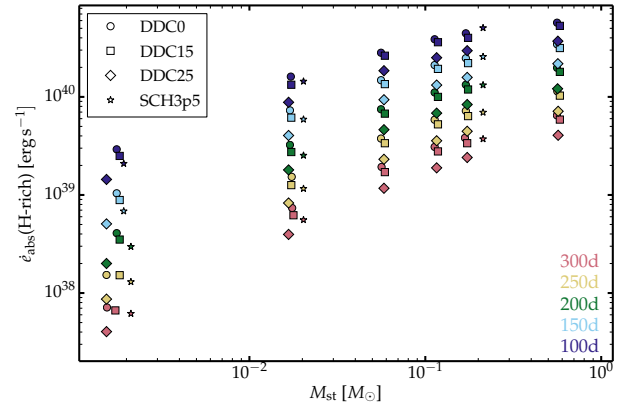


Fig. 14. Decay power absorbed by the stripped material vs. its mass for our set of models. As before, the color coding distinguishes the SN ages, which cover from 100 to 300 d. The decay power absorbed is greater at earlier times (because the total decay power is greater earlier) or for greater masses of stripped material (because of the greater trapping). However, this does not imply that the $H\alpha$ line is more easily seen earlier since the SN luminosity is also greater. The line luminosity may be high but the equivalent width, or pseudo-equivalent width, may be small and even null.

by the stripped material is radiated by other means. A fraction of this power goes in lines, and the rest in continuum radiation (see Fig. 4 for one representative case). Alternatively, we could quote the $H\alpha$ luminosity from the total emergent spectrum. This is more useful to compare to observations, but prevents a proper evaluation of the cooling power of $H\alpha$ since the $H\alpha$ emission from the stripped material is reprocessed by the metal-rich ejecta.

The fraction $L(H\alpha)/\dot{\epsilon}_{\text{abs}}(\text{H-rich})$ of about 10% holds over three orders of magnitude in decay power absorbed by the stripped material. This is lower than the value of 30% found by Botyánszki et al. (2018) for most of their models.

8.3. Evolution of the $H\alpha$ luminosity

We have seen that the $H\alpha$ luminosity represents about 10% of the decay power absorbed (Fig. 13). This dependence implies a

connection to the ^{56}Co characteristic decay time. However, there are a number of complications that can yield an $H\alpha$ luminosity that deviates from the evolution of the decay power emitted or absorbed. These complications can be, for example, a different luminosity evolution for the metal-rich ejecta and for the stripped material, combined with the evolution of the blanketing effect from the metal-rich ejecta.

The top and middle panels of Fig. 15 show the evolution of the $H\alpha$ luminosity for M_{st} of 0.0018, 0.018, and $0.18 M_{\odot}$, first based on the H I spectrum and then based on a difference between the model counterparts with $M_{\text{st}} = 10^{-5} M_{\odot}$. This evolution is smooth and qualitatively similar for all cases, largely irrespective of ^{56}Ni mass. However, the models with lower M_{st} decline faster, along a nearly constant slope (in the log, so in magnitude). The models with a higher M_{st} show a plateau from 100 to 200 d (or even a rise if the flux difference is used), and then decline, but more slowly. The different behavior seen at early times in both panels arises from optical depth effects. It shows that up to 200 d, a very slow decline in the $H\alpha$ luminosity can arise even if the power source is ^{56}Co decay; it does not necessarily imply CSM interaction, as proposed by Valley et al. (2019).

When normalized to the bolometric luminosity (which is equal to the total decay power absorbed at these late epochs), the $H\alpha$ luminosity is constant or growing for models with a high M_{st} but decreases with time otherwise. This is in part related to the fact that at low M_{st} , γ -rays are not efficiently trapped by the stripped material, while the SN Ia ejecta are increasingly powered by local positron energy (which the stripped material cannot receive since it is ^{56}Ni deficient). A corollary is that the stripped material allows the SN to be more luminous since it contributes to trapping γ -rays that would have otherwise escaped. This is not necessarily seen in $H\alpha$, but may yield a continuum flux excess throughout the optical. This is visible in the bottom-row panels of Fig. 5 where the models with higher M_{st} are offset to higher luminosities at all wavelengths, not just in strong lines like $H\alpha$.

In the upper panel of Fig. 15, we computed the line luminosity from the H I spectrum in order to understand how this luminosity evolves without the corrupting effect of photon reprocessing by the metal-rich ejecta. However, this reprocessing is moderate after about 200 d for $H\alpha$. After that time, the results shown in Fig. 15 reflect closely the evolution of the emergent $H\alpha$ luminosity (see Fig. 8).

8.4. $H\alpha$ versus $H\beta$ luminosities

Figure 16 shows the ratio of $H\alpha$ and $H\beta$ line luminosities computed from the H I-only spectrum. Apart from cases of very low M_{st} , the ratio is not strongly dependent on M_{st} but it varies strongly with time, increasing from about 2 at 100 d up to 10–20 at 300 d. Such a Balmer decrement is much greater than the value of 2.86 for Case B recombination (Osterbrock & Ferland 2006) but the conditions here are also very different from those in a photoionized nebula.

A fundamental difference in SNe Ia with stripped material is that the nebula is powered not by ionizing photons from a hot central star but instead from within the ejecta and by radioactive decay. The associated non-thermal effects influence both the excitation and ionization of H and other elements. The process is therefore quite different from photoionization followed by recombination.

The detectability of $H\beta$ in the total emergent spectrum is another issue. As discussed earlier, the blanketing by the metal-rich ejecta affects the Balmer decrement severely in our

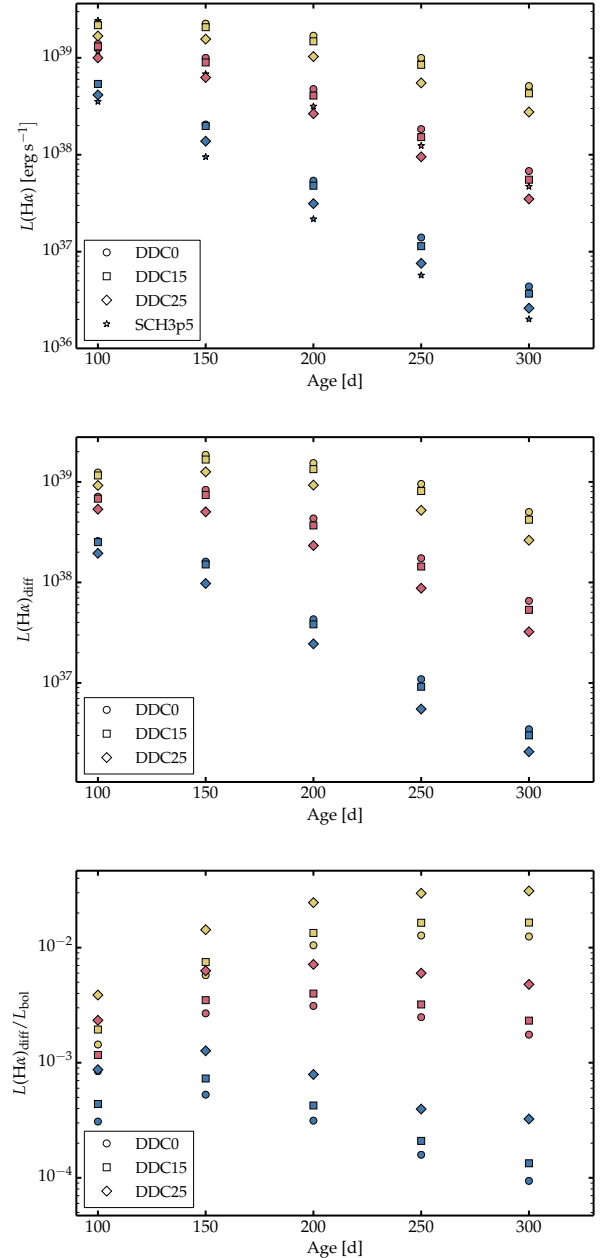


Fig. 15. Evolution with SN age of the $H\alpha$ luminosity (top and middle) or the normalized $H\alpha$ luminosity (bottom) for a subset of models covering stripped material masses of about 0.0018 (blue), 0.018 (red), and $0.18 M_{\odot}$ (yellow). For the two lower panels, the $H\alpha$ flux is calculated by integrating over $H\alpha$ after subtracting the flux from the corresponding reference model with $M_{\text{st}} = 10^{-5} M_{\odot}$. For the top panel, the $H\alpha$ flux is calculated from the H I spectrum. The different behavior with stripped material masses arises from optical depth effects, which are important in the time span 100–200 d here. These effects can produce an $H\alpha$ luminosity that evolves very differently from that expected for ^{56}Co decay, even though ^{56}Co decay is the power source for the emission from the stripped material.

simulations. Consequently, $H\beta$ is absent or very weak in our simulations of the total emergent spectrum.

9. Equivalent width of the $H\alpha$ line

Unlike luminosity, the equivalent width (EQW) of an emission line – or, more commonly here, an upper limit on its possible

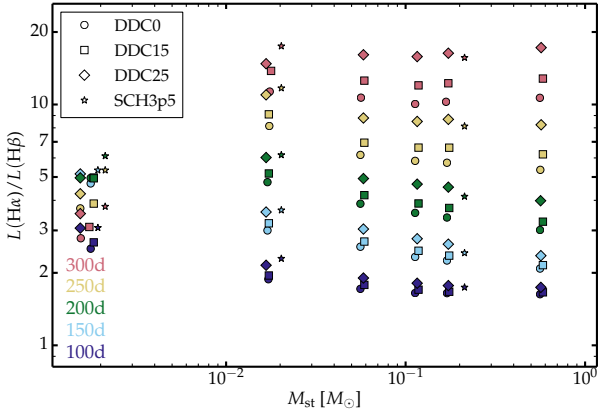


Fig. 16. Ratio of the $H\alpha$ to $H\beta$ luminosity for our set of models, adopting only H I lines in the spectrum calculation. Values are scattered, reflecting the influence of intrinsic optical depth effects and the non-thermal process of formation of these lines. This ratio ignores optical depth effects caused by other elements such as iron. Consequently, in the total emergent spectrum (resulting from the contribution of all elements and ions), this ratio is much greater, and potentially infinite.

strength – is a quantity that is directly derivable from an observed SN spectrum. That is, it is independent of the SN brightness, distance, and extinction, all of which are required to establish the luminosity of such a line or to place limits on it. Indeed, for all but two of the more than 100 nebular-phase SNe Ia that have so far had their spectra scrutinized for evidence of stripped material, it is an upper limit on the EQW of a line that has served as the fundamental, measured parameter that is derived from the spectrum itself.

Because our models compute the full, nebular-phase SN Ia spectrum in addition to the expected emergent line luminosities produced by stripped material, they permit estimates of specific line EQWs to be made. This can potentially be used to directly assess – or to place limits on – the amount of stripped material entrained in an SN ejecta without requiring contemporaneous photometry or estimates of its distance and extinction.

With this in mind, we measured the EQW of the $H\alpha$ line – hereafter $\text{EQW}(H\alpha)$ – in all of our Chandrasekhar-mass model spectra using a procedure designed to mimic its derivation from an actual SN spectrum. First, to approximate the “continuum” underlying the emission line, points on the spectrum shortwards and longwards of the $H\alpha$ feature were chosen by hand and connected with a linear fit². The line’s emission profile was then normalized through division by this fitted continuum. We then calculated $\text{EQW}(H\alpha)$ by taking the normalized flux, subtracting one from it, and summing the flux up over the range 6541–6585 Å. This range encompasses nearly all of the line emission (Fig. 5), as it includes $\pm 1000 \text{ km s}^{-1}$ from the nominal line center.

We display the results in Fig. 17 for all models containing more than $0.001 M_{\odot}$; for the two models that contained less than this – $M_{\text{st}} = 1.7 \times 10^{-4} M_{\odot}$ and $M_{\text{st}} = 1.7 \times 10^{-5} M_{\odot}$ – the $H\alpha$ line was very difficult to measure (if apparent at all), and in all measured cases yielded $\text{EQW}(H\alpha) < 1 \text{ \AA}$. From the

² This interactive approach was chosen over subtracting a model with essentially zero stripped matter (i.e., the model with $M_{\text{st}} = 0.000017 M_{\odot}$) since small amounts of “continuum” were added by the stripped material (see Fig. 3) and we wished to reproduce, as closely as possible, the procedure applied to an actual SN spectrum. In most cases, the difference was very small.

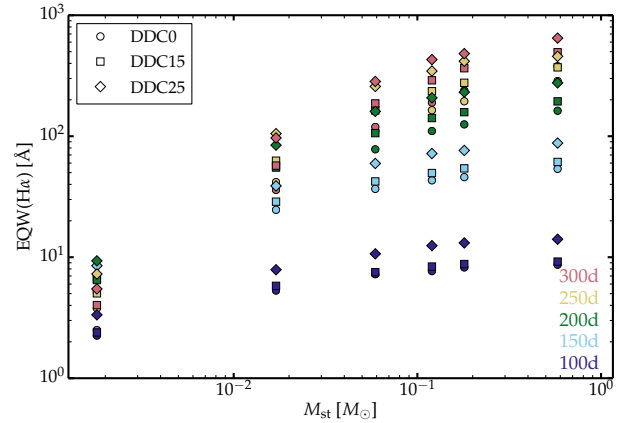


Fig. 17. Variation of the $H\alpha$ equivalent width, measured in the emergent spectrum, as a function of stripped-material mass, M_{st} , for our set of Chandrasekhar-mass delayed detonation models (DDC0, DDC15, and DDC25). Color coding defines the SN age.

figure, three trends are immediately apparent. First, $\text{EQW}(H\alpha)$ increases with M_{st} at all epochs and for all models. Second, $\text{EQW}(H\alpha)$ increases with decreasing ^{56}Ni mass at all epochs. This arises primarily because of the reduced light contamination from the SN ejecta for lower ^{56}Ni mass (this contamination corresponds to the “pseudo-continuum” by which we normalize the flux when measuring the EQW). Finally, it increases with time for all models with $M_{\text{st}} \geq 0.059 M_{\odot}$, consistent with our earlier finding that when sufficient stripped material exists it receives an increasing fraction of the decay power relative to the metal-rich ejecta (Sect. 3). However, $\text{EQW}(H\alpha)$ does exhibit more complicated temporal behavior for the two models with lower M_{st} . While it generally increases up to day ~ 200 , it levels off, or even decreases, beyond that time. As discussed in Sect. 8.3, this is likely related to the decreasing efficiency of γ -ray trapping by the stripped material at low M_{st} . We provide analytical fits to the correlations between $\text{EQW}(H\alpha)$ and M_{st} in Appendix B, along with a suggested prescription for deriving conservative limits on the line’s possible strength in observed SN Ia spectra.

The essential results of this exercise can be summarized succinctly. First, if a late-time SN Ia spectrum is obtained with sufficient sensitivity to rule out any $H\alpha$ emission for which $\text{EQW}(H\alpha) \geq 1 \text{ \AA}$, a confident limit can be set on the amount of stripped material of $M_{\text{st}} < 0.001 M_{\odot}$, which is well below the amount expected in the single-degenerate scenario. Second, balancing the changing effects of relative $H\alpha$ strength, a fading SN and line luminosity, and opacity effects at low M_{st} , suggests that the ideal time period to obtain spectra and seek $H\alpha$ emission lies between days ~ 150 and 200.

10. Conclusions

We have presented a grid of radiative transfer calculations for SN Ia ejecta that enclose some stripped material from a non-degenerate companion star. Our set of models covers from faint to luminous SNe Ia, to test the influence of ^{56}Ni , as well as M_{ch} and sub- M_{ch} progenitors to test the influence of the ejecta mass on the results. The ejecta structure is spherically symmetric and parametrized, but uses some constraints from multidimensional hydrodynamics simulations. We extend previous calculations by covering a broader parameter space, by treating the non-LTE radiative-transfer problem in detail. Optical depth effects are treated. The influence of the fast-moving metal-rich ejecta on the

radiation emanating from the slower moving stripped material is treated. We cover a range of stripped material masses, from the values of $0.1\text{--}0.5 M_{\odot}$ obtained in multidimensional hydrodynamics simulations down to the low values of about $0.001 M_{\odot}$ that have been inferred from observations.

Our simulations suggest that the emission from the stripped material first appears in the emergent spectrum some time between 50 and 100 d after explosion for the largest values of M_{st} . This delay is wavelength dependent and results from a combination of effects. Metal-line blanketing blocks the radiation from the stripped material in the region below about 5000 \AA as well as in isolated regions (for example over the near infrared Ca II triplet). This prevents the emergence of H β photons even at 300 d (the associated Balmer decrement is thus infinite). In contrast, H α emerges much earlier (for example around 100 d for $M_{\text{st}} \sim 0.1 M_{\odot}$) because it sits in a spectral region that is relatively free of optically thick metal lines. The same holds for lines like He I $1.083 \mu\text{m}$ or O I $1.129 \mu\text{m}$. The second effect is related to the brightness contrast between the emission from the stripped material and that of the overlying metal-rich ejecta. At earlier times, the metal-rich ejecta outshine the stripped material and makes its detection challenging. The problem is less severe for H α because it is intrinsically the strongest optical emission line radiated by the stripped material but also because it is located in a spectral region where the metal-rich ejecta have a moderate brightness. Because of these two effects, H α remains the main observable signature from the stripped material at any ultraviolet, optical, or near-infrared wavelength.

At a given time, the H α luminosity increases with M_{st} because of the greater decay power absorbed by the stripped material (in all our simulations, about 10% of this power is radiated by H α). Being powered by radioactive decay, the H α luminosity generally decreases with time, but this drop is steeper for lower M_{st} because these configurations are less efficient at trapping γ -rays. Growing γ -ray escape from the metal-rich ejecta favors the strengthening of H α , which becomes the strongest optical line in our simulations at 300 d for large M_{st} . Prior to 200 d, the H α luminosity can exhibit different behaviors (plateau, rise, or drop), primarily because of optical depth effects. The EQW(H α) is found to increase with M_{st} , increase with decreasing ^{56}Ni mass, and generally increase with time except at the lower values of M_{st} .

Optical depth effects significantly impact the radiation from SN Ia ejecta with stripped material. The Balmer lines are intrinsically optically thick even at 300 d, and emission from the stripped material is also attenuated by the metal-rich ejecta. Optical depth effects caused by the metal-rich ejecta are a fundamental feature of SN Ia with stripped material. These effects are in a large part absent from SN Ia ejecta interacting with CSM since the emission is external to the ejecta rather than deeply embedded within it (optical depth effects influence the receding part of the ejecta but leave intact the front part).

There seems to be a number of ways to distinguish SN Ia ejecta with stripped material and those with CSM interaction. With CSM interaction, H α is observed earlier (it may be observed at any time), H β is often detected even at the earliest times (see for example Hamuy et al. 2003 and Silverman et al. 2013), the CSM revealed by high-resolution spectroscopy moves slowly (100 km s^{-1} ; Kotak et al. 2004), and there may be the presence of symmetric electron-scattering wings on H α . With $0.1\text{--}0.5 M_{\odot}$ of stripped material as predicted by hydrodynamical simulations (see for example Marietta et al. 2000), Balmer lines cannot be seen much earlier than 100 d after explosion, H α should strengthen with time relative to the rest of the optical

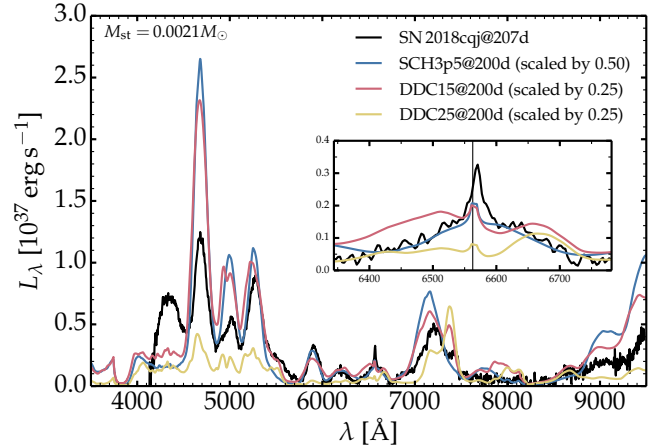


Fig. 18. Comparison of the luminosity of model SCH3p5, DDC15, and DDC25 with $M_{\text{st}} = 0.0021 M_{\odot}$ at 200 d to the observations of SN 2018cjq at 207 d after explosion. Data as well as SN distance, reddening, and redshift are taken from Prieto et al. (2020). The model luminosities are scaled by various amounts (see label).

spectrum, H β and higher transitions in the series should not be detected during the first year, and H α should be broader but cannot exhibit symmetric electron scattering wings.

Overall, our simulations are in rough agreement with the previous works of Mattila et al. (2005) and Botyánszki et al. (2018). However, our results suggest that optical depth effects produce some important signatures and thus should not be neglected. We also predict weak or absent He I lines for stripped material with a solar composition, with the exception of He I 10830 \AA , in tension with the numerous optical He I lines predicted by Botyánszki et al. (2018). This may be caused by the different non-thermal and non-LTE treatment, and the neglect of optical depth effects.

The junction between optical and near infrared ranges might also reveal some interesting properties. Since metal-line blanketing is weak in this region, the stripped material can be seen through H I, He I, or O I lines. It is not clear whether such lines are predicted in the case of CSM interaction or whether they have ever been observed in SNe Ia with H α detection.

The hydrodynamical models of stripped material from a companion in a SN Ia seem unsuited to explain the observations of SNe Ia with an H α detection (this discrepancy, however, could be resolved by adopting different, and perhaps more physical, initial conditions for the companion, non-degenerate star at the time of explosion; see for example Justham 2011). Even with the large uncertainties inherent to the radiative transfer calculations, these inferred masses are typically 100 times smaller than predicted by hydrodynamical simulations (Kollmeier et al. 2019; Prieto et al. 2020). Figure 18 compares one of our calculations with M_{st} of about $0.002 M_{\odot}$ to the observations of SN 2018cjq at about 200 d, yielding a good overall match but requiring a very low value for M_{st} .

An alternative scenario for the production of H α is interaction with an extended H-rich CSM, so that H α is detected some time after the SN Ia explosion and ceases after a few months once the CSM has been swept up completely by the ejecta. Variations in CSM density structure (or wind mass rate of the progenitor) could yield a wide range of H α luminosities, both in value at a given time and in the evolution of this value until late times. Another possibility, tied to the double-degenerate scenario, is that the inferred $0.001 M_{\odot}$ of H-rich material at low velocity could come from a swept-up giant planet (Soker 2019), or from a

non-degenerate star in a triple system (Thompson 2011; Kushnir et al. 2013; Valley et al. 2019).

The properties of SNe Ia with $H\alpha$ emission reveal an intriguing dichotomy. Events that exhibit strong $H\alpha$ are associated with SNe Ia having a high peak luminosity (or high ^{56}Ni mass), interacting with a dense H-rich CSM, and are located in relatively young stellar populations. In contrast, the two events that exhibit weak $H\alpha$ emission are associated with SNe Ia with faint peak luminosity (or low ^{56}Ni mass), have fast-declining light curves, and are located in relatively old stellar populations. There is a dearth of events in between these two extremes. Detectability might play a role here (detecting a weak $H\alpha$ is easier at low ^{56}Ni ; see Sect. 9), but this is probably not the core reason. A distinct progenitor or explosion scenario may be the cause (see, for example, Kollmeier et al. 2019; Valley et al. 2019).

A final issue not directly addressed in studies of SNe Ia with $H\alpha$ detection is whether Chandrasekhar-mass ejecta are suitable to explain the nebular properties of the SN in terms of brightness, color, ionization, line ratios, and other factors. There is indeed growing evidence that the majority of SNe Ia are better explained by the properties of sub-Chandrasekhar-mass ejecta (see, for example, van Kerkwijk et al. 2010; Kromer et al. 2010; Kushnir et al. 2013; Pakmor et al. 2013; Scalzo et al. 2014; Blondin et al. 2017, 2018; Botyánszki et al. 2018; Shen et al. 2018; Flörs et al. 2019; Polin et al. 2019; Wygoda et al. 2019). In Fig. 18, a sub-Chandrasekhar-mass model yields a better match to the observed optical spectrum and brightness than a Chandrasekhar-mass model with a comparable ^{56}Ni mass. The single-degenerate scenario, intimately tied to the Chandrasekhar-mass for the exploding white dwarf, seems to struggle both in matching the observed $H\alpha$ line strength and the optical radiation from the metal-rich ejecta.

Acknowledgements. Support for J.L.P. is provided in part by FONDECYT through the grant 1191038 and by the Ministry of Economy, Development, and Tourism's Millennium Science Initiative through grant IC120009, awarded to The Millennium Institute of Astrophysics, MAS. This work was granted access to the HPC resources of CINES under the allocations 2018 – A0050410554 and 2019 – A0070410554 made by GENCI.

References

- Anderson, J. P., Dessart, L., Gutierrez, C. P., et al. 2014, *MNRAS*, 441, 671
- Blondin, S., Dessart, L., Leibundgut, B., et al. 2006, *AJ*, 131, 1648
- Blondin, S., Dessart, L., Hillier, D. J., & Khokhlov, A. M. 2013, *MNRAS*, 429, 2127
- Blondin, S., Dessart, L., & Hillier, D. J. 2015, *MNRAS*, 448, 2766
- Blondin, S., Dessart, L., Hillier, D. J., & Khokhlov, A. M. 2017, *MNRAS*, 470, 157
- Blondin, S., Dessart, L., & Hillier, D. J. 2018, *MNRAS*, 474, 3931
- Botyánszki, J., & Kasen, D. 2017, *ApJ*, 845, 176
- Botyánszki, J., Kasen, D., & Plewa, T. 2018, *ApJ*, 852, L6
- Chugai, N. N. 1986, *Sov. Astron.*, 30, 563
- Dessart, L., & Hillier, D. J. 2005, *A&A*, 437, 667
- Dessart, L., & Hillier, D. J. 2011, *MNRAS*, 410, 1739
- Dessart, L., Hillier, D. J., Waldman, R., & Livne, E. 2013, *MNRAS*, 433, 1745
- Dessart, L., Hillier, D. J., Blondin, S., & Khokhlov, A. 2014a, *MNRAS*, 441, 3249
- Dessart, L., Blondin, S., Hillier, D. J., & Khokhlov, A. 2014b, *MNRAS*, 441, 532
- Dimitriadis, G., Rojas-Bravo, C., Kilpatrick, C. D., et al. 2019, *ApJ*, 870, L14
- Flörs, A., Spyromilio, J., Taubenberger, S., et al. 2019, *MNRAS*, 491, 2902
- Graham, M. L., Kumar, S., Hosseinzadeh, G., et al. 2017, *MNRAS*, 472, 3437
- Hachisu, I., Kato, M., & Nomoto, K. 2008, *ApJ*, 679, 1390
- Hachisu, I., Kato, M., & Nomoto, K. 2012, *ApJ*, 756, L4
- Hamuy, M., Phillips, M. M., Suntzeff, N. B., et al. 2003, *Nature*, 424, 651
- Hillier, D. J., & Dessart, L. 2012, *MNRAS*, 424, 252
- Hillier, D. J., & Miller, D. L. 1998, *ApJ*, 496, 407
- Hobbs, L. M. 1984, *ApJ*, 280, 132
- Holmbo, S., Stritzinger, M. D., Shappee, B. J., et al. 2019, *A&A*, 627, A174
- Jerkstrand, A., Fransson, C., Maguire, K., et al. 2012, *A&A*, 546, A28
- Justham, S. 2011, *ApJ*, 730, L34
- Kollmeier, J. A., Chen, P., Dong, S., et al. 2019, *MNRAS*, 486, 3041
- Kotak, R., Meikle, W. P. S., Adamson, A., & Leggett, S. K. 2004, *MNRAS*, 354, L13
- Kozma, C., Fransson, C., Hillebrandt, W., et al. 2005, *A&A*, 437, 983
- Kromer, M., Sim, S. A., Fink, M., et al. 2010, *ApJ*, 719, 1067
- Kushnir, D., Katz, B., Dong, S., Livne, E., & Fernández, R. 2013, *ApJ*, 778, L37
- Leonard, D. C. 2007, *ApJ*, 670, 1275
- Leonard, D. C., & Filippenko, A. V. 2001, *PASP*, 113, 920
- Li, C., Hillier, D. J., & Dessart, L. 2012, *MNRAS*, 426, 1671
- Liu, Z.-W., & Stancliffe, R. J. 2017, *MNRAS*, 470, L72
- Liu, Z. W., Pakmor, R., Röpke, F. K., et al. 2012, *A&A*, 548, A2
- Lundqvist, P., Mattila, S., Sollerman, J., et al. 2013, *MNRAS*, 435, 329
- Lundqvist, P., Nyholm, A., Taddia, F., et al. 2015, *A&A*, 577, A39
- Maguire, K., Taubenberger, S., Sullivan, M., & Mazzali, P. A. 2016, *MNRAS*, 457, 3254
- Marietta, E., Burrows, A., & Fryxell, B. 2000, *ApJS*, 128, 615
- Mattila, S., Lundqvist, P., Sollerman, J., et al. 2005, *A&A*, 443, 649
- Nomoto, K., Thielemann, F. K., & Yokoi, K. 1984, *ApJ*, 286, 644
- Osterbrock, D. E., & Ferland, G. J. 2006, *Astrophysics of Gaseous Nebulae and Active Galactic Nuclei* (Sausalito, CA: University Science Books)
- Pakmor, R., Röpke, F. K., Weiss, A., & Hillebrandt, W. 2008, *A&A*, 489, 943
- Pakmor, R., Kromer, M., Taubenberger, S., & Springel, V. 2013, *ApJ*, 770, L8
- Pan, K.-C., Ricker, P. M., & Taam, R. E. 2010, *ApJ*, 715, 78
- Pan, K.-C., Ricker, P. M., & Taam, R. E. 2012, *ApJ*, 750, 151
- Polin, A., Nugent, P., & Kasen, D. 2019, *ApJ*, 873, 84
- Press, W. H., Teukolsky, S. A., Vetterling, W. T., & Flannery, B. P. 1992, *Numerical Recipes in C. The art of Scientific Computing* (Cambridge: Cambridge University Press)
- Prieto, J. L., Chen, P., Dong, S., et al. 2020, *ApJ*, 889, 100
- Sand, D. J., Graham, M. L., Botyánszki, J., et al. 2018, *ApJ*, 863, 24
- Sand, D. J., Amaro, R. C., Moe, M., et al. 2019, *ApJ*, 877, L4
- Scalzo, R. A., Ruitter, A. J., & Sim, S. A. 2014, *MNRAS*, 445, 2535
- Shappee, B. J., Stanek, K. Z., Pogge, R. W., & Garnavich, P. M. 2013, *ApJ*, 762, L5
- Shappee, B. J., Piro, A. L., Stanek, K. Z., et al. 2018, *ApJ*, 855, 6
- Shen, K. J., Kasen, D., Miles, B. J., & Townsley, D. M. 2018, *ApJ*, 854, 52
- Silverman, J. M., Nugent, P. E., Gal-Yam, A., et al. 2013, *ApJS*, 207, 3
- Silverman, J. M., Pickett, S., Wheeler, J. C., et al. 2017, *MNRAS*, 467, 369
- Soker, N. 2019, *Res. Notes Am. Astron. Soc.*, 3, 153
- Swartz, D. A., Sutherland, P. G., & Harkness, R. P. 1995, *ApJ*, 446, 766
- Thompson, T. A. 2011, *ApJ*, 741, 82
- Tucker, M. A., Shappee, B. J., & Wisniewski, J. P. 2019, *ApJ*, 872, L22
- Tucker, M. A., Shappee, B. J., Valley, P. J., et al. 2020, *MNRAS*, 493, 1044
- Valley, P. J., Fausnaugh, M., Jha, S. W., et al. 2019, *MNRAS*, 487, 2372
- van Kerkwijk, M. H., Chang, P., & Justham, S. 2010, *ApJ*, 722, L157
- Wheeler, J. C., Lecar, M., & McKee, C. F. 1975, *ApJ*, 200, 145
- Wilk, K. D., Hillier, D. J., & Dessart, L. 2019, *MNRAS*, 487, 1218
- Wilk, K. D., Hillier, D. J., & Dessart, L. 2020, *MNRAS*, 494, 2221
- Wygoda, N., Elbaz, Y., & Katz, B. 2019, *MNRAS*, 484, 3941
- Zhang, T., Wang, X., Wu, C., et al. 2012, *AJ*, 144, 131

Appendix A: Analytical fits to the correlation between H α luminosity and M_{st}

Table A.1. Coefficients of the polynomial fits to the correlation between H α luminosity and M_{st} for the models DDC0, DDC15, and DDC25 at 100, 150, 200, 250, and 300 d.

Model	Age [d]	a_0	a_1	a_2
DDC0	100	39.15	-0.01	-0.10
DDC0	150	39.34	-0.05	-0.17
DDC0	200	39.35	0.04	-0.21
DDC0	250	39.25	0.19	-0.21
DDC0	300	39.04	0.29	-0.21
DDC15	100	39.11	-0.02	-0.10
DDC15	150	39.31	-0.02	-0.16
DDC15	200	39.30	0.07	-0.20
DDC15	250	39.16	0.15	-0.24
DDC15	300	38.97	0.30	-0.22
DDC25	100	39.01	-0.01	-0.09
DDC25	150	39.22	0.06	-0.14
DDC25	200	39.19	0.17	-0.17
DDC25	250	39.01	0.22	-0.21
DDC25	300	38.79	0.37	-0.18

Notes. The polynomial has the form $Y = a_0 + a_1X + a_2X^2$, where $Y = \log_{10}(L(\text{H}\alpha)_{\text{diff}}/\text{erg s}^{-1})$ and $X = \log_{10}(M_{\text{st}}/M_{\odot})$.

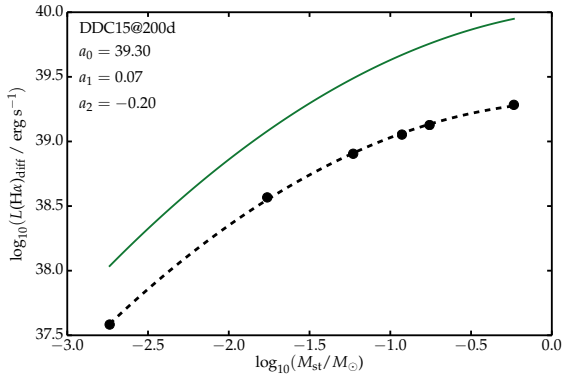


Fig. A.1. Illustration of the polynomial fit (black dashed line) to the distribution of H α luminosity and M_{st} (filled dots) for the model DDC15 at 200 d, together with the correlation obtained by Botyánszki et al. (2018) for their models at 200 d. Their Eq. (1) should read $Y = 40.0 + 0.17X - 0.2X^2$, with the nomenclature given in the caption of our Table A.1 above.

It is useful to perform polynomial fits to our results for the H α luminosity for the various models, epochs, and stripped material masses. Maintaining the same approach as used in Botyánszki et al. (2018), we fit a second order polynomial to the distribution of H α luminosity versus M_{st} at each epoch and for each model (which reflects a given ^{56}Ni mass). The results for the polynomial coefficients are given in Table A.1 and an illustration of the fit for model DDC15 at 200 d (which corresponds to the configuration closest to that of Botyánszki et al. 2018) is shown in Fig. A.1.

Appendix B: EQW (H α) versus M_{st} , and an H α detection-limit prescription

We have fit polynomials to our results for EQW(H α) in a manner identical to those fitted to its luminosity (see Appendix A).

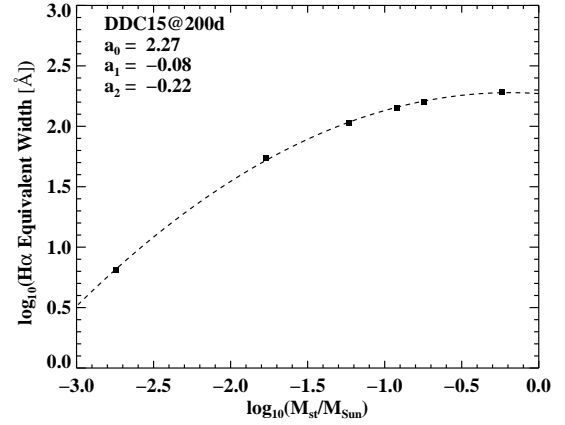


Fig. B.1. Example of the polynomial fit (black dashed line) to the distribution of measured H α equivalent width at simulated values of M_{st} for the model DDC15 at 200 d. The caption to Table B.1 gives the definitions of a_0 , a_1 , a_2 .

Table B.1. Coefficients of the polynomial fits to the correlation between H α equivalent width and M_{st} for the models DDC0, DDC15, and DDC25 at 100, 150, 200, 250, and 300 days.

Model	Age [d]	a_0	a_1	a_2
DDC0	100	0.93	-0.06	-0.10
DDC0	150	1.70	-0.09	-0.16
DDC0	200	2.22	0.01	-0.20
DDC0	250	2.50	0.11	-0.21
DDC0	300	2.65	0.20	-0.23
DDC15	100	0.95	-0.07	-0.10
DDC15	150	1.76	-0.09	-0.16
DDC15	200	2.27	-0.08	-0.22
DDC15	250	2.58	0.00	-0.25
DDC15	300	2.75	0.09	-0.25
DDC25	100	1.15	-0.01	-0.09
DDC25	150	1.92	-0.09	-0.16
DDC25	200	2.41	-0.14	-0.24
DDC25	250	2.63	-0.20	-0.31
DDC25	300	2.81	-0.07	-0.30

Notes. The polynomial has the form $Y = a_0 + a_1X + a_2X^2$, where $Y = \log_{10}(\text{EQW}(\text{H}\alpha)/\text{\AA})$ and $X = \log_{10}(M_{\text{st}}/M_{\odot})$.

Figure B.1 provides an illustration of the fit for our standard explosion model DDC15 at 200 d. The polynomial coefficients for all models are reported in Table B.1.

Past research tells us that it is nearly always an upper limit, and not a detection, that is established on the strength of the H α line. The procedure for estimating an upper limit on a line's possible strength – as measured by the EQW – has evolved over the years. The basic methodology was proposed by Leonard & Filippenko (2001) based on the seminal work of Hobbs (1984). The technique was then implemented specifically for the case of nebular-phase SNe Ia by Leonard (2007). A subsequent empirical investigation by Sand et al. (2018), in which artificial emission lines were directly injected into actual SN spectra and then recovered, yielded changes to both the technique and statistical inferences drawn from it; further refinements were also contributed by Tucker et al. (2020) based in part on the work of Maguire et al. (2016). Adopting the accepted, and most conservative, practices from all of the above work together with

the present paper’s results yields the following recommended procedure.

1. Obtain a high S/N spectrum centered on $H\alpha$ at as high a resolution as possible (resolutions of at least $\sim 3 \text{ \AA}$ are desirable to resolve potentially narrow features, since the line width is expected to have a viewing-angle dependence) more than 100 days post-explosion; epochs between 150 and 200 days are particularly desirable.
2. Remove the redshift and rebin the spectrum to the resolution delivered by the spectrograph (as derived, for example, through measurements of widths of night-sky lines).
3. Fit a second-order Savitsky-Golay smoothing polynomial (Press et al. 1992) of width $\sim 70 \text{ \AA}$ to the spectrum, taking care to exclude the region from 6541–6585 \AA to prevent biasing the continuum fit in the event $H\alpha$ may be detectable. Apply a 3σ clipping to the continuum data regions to exclude any artifacts. If any pixels in the nominal $H\alpha$ region are deemed to be untrustworthy (due to, e.g., host-galaxy contamination, telluric absorption, or instrumental artifacts), apply the pixel-masking technique described by Tucker et al. (2020).
4. Normalize the spectrum by dividing it by the smoothed continuum, and calculate the 1σ rms fluctuation of the flux around the normalized continuum.
5. Difference the smoothed and unsmoothed spectra, and examine the residuals for narrow emission near $H\alpha$. In the event no emission is detected, calculate an upper limit on its presence through

$$\text{EQW}(H\alpha) < 12\Delta I \sqrt{W_{\text{line}}\Delta\lambda}, \quad (\text{B.1})$$
 where ΔI is the 1σ rms fluctuation of the flux around the normalized continuum level, $\Delta\lambda$ is the resolution of the spectrum in \AA (which has been set equal to the width of each spectral bin), W_{line} is the full width at half maximum of the expected feature, typically taken to be 22 \AA ($\sim 1000 \text{ km s}^{-1}$), and $\text{EQW}(H\alpha)$ is the derived upper bound on the equivalent width of the undetected $H\alpha$ feature.
6. Use the derived limit on $\text{EQW}(H\alpha)$ to estimate the maximum M_{st} whose effects could remain “hidden” in the spectrum. This may be done by using the fits given in Table B.1 for the epoch and model of choice (i.e., DDC0 for overluminous, DDC15 for normally bright, and DDC25 for subluminous). As a simple rule of thumb, if $\text{EQW}(H\alpha) \lesssim 1 \text{ \AA}$ at any epoch > 100 days, then $M_{\text{st}} > 0.001 M_{\odot}$ can be confidently ruled out for all models.